

FACULTY OF SCIENCE  
UNIVERSITY OF COPENHAGEN



# Master's thesis

Nastasia Okulova

## Spin qubit devices in GaAs

Towards improving operation, coupling and sensing

Academic advisor:  
Prof. Charles Marcus  
Submitted: 02.01.2015

Institutnavn: Niels Bohr Institute

Name of department: Center for Quantum Devices

Author: Nastasia Okulova

Titel og evt. undertitel: Spin kvantebit enheder i GaAs, hen mod forbedring af kontrol og ,kobling og udlæsning

Title / Subtitle: Spin qubit devices in GaAs: towards improving operation coupling and sensing

Subject description: Fabrication of spin qubit devices on GaAs heterostructures, characterisation and measurement the produced samples.

Academic advisor: Charles Marcus

Submitted: 2<sup>nd</sup> January 2014

Grade:

## Table of Contents

List of figures.....	4
Abstract.....	5
Acknowledgements.....	6
Introduction.....	7
Chapter 1. Background.....	10
1.1 Quantum bit of information.....	10
1.2 Quantum dots and qubit implementations.....	12
1.4 Qubits in three quantum dots.....	17
Chapter 2. Preparations for the experiment.....	23
2.1 Designing the gate pattern.....	23
2.2 Fabrication on GaAs/AlGaAs heterostructures.....	27
2.3 The story of Magnets.....	34
2.4 Contacting the macro world: Circuit Boards.....	36
2.5 Dilution refrigerator.....	38
2.6 Measurement setup.....	41
Chapter 3. Measurement techniques.....	44
3.1 Bias cooling and testing the device performance.....	44
3.2 Transport through a quantum dot.....	46
3.3 Charge sensing.....	47
3.4 Reflectometry and pulsing.....	48
Chapter 4. Results and experiences.....	52
4.1 Repeating the past experiments.....	53
4.2 Adding a third dot.....	57
4.3 The coupler.....	59
4.5 Summary of other experiences.....	59
Chapter 5. Summary and outlook.....	62
5.1 Summary of the results and experiences.....	62
5.2 Suggestions for the improvements.....	63
5.3 Conclusion.....	64
Appendix A. Fabrication Recipe.....	65
Repeated actions.....	65
Exposing Ohmics or outer connection layer.....	65
Fine gates in the E-line.....	65
Appendix B. Cooled down devices, bonding schemes, boards.....	77
Fabricated samples:.....	77
The cooled down devices:.....	78
Appendix C. Pin-out for the Sydney board.....	79
Bibliography.....	80

## List of figures

Figure 1. The Block sphere.....	10
Figure 2. Laterally defined quantum dot.....	12
Figure 3. Two-dimensional electron gas.....	13
Figure 4. Metallic gates, depletion of the 2DEG.....	14
Figure 5. Coulomb and spin blockade.....	15
Figure 6. Triple quantum dots.....	18
Figure 7. Asymmetrical triple dot with a multi-electron dot in the left dot position.....	21
Figure 8. SEM images, evolution of the gate designs over time.....	26
Figure 9. A complete fabricated device.....	27
Figure 10. E-beam lithography.....	29
Figure 11. The design for fabrication process.....	31
Figure 12. Wrong dose used for the fabrication.....	32
Figure 13. Single pixel line gates produced with E-line and Elionix.....	33
Figure 14. Cross-linked resist after SEM imaging of the devices.....	34
Figure 15. Misshaped magnets.....	35
Figure 16. The Mayo board and Sydney sample board.....	36
Figure 17. The Sydney board mounted into the puck.....	37
Figure 18. The layout of the Oxford Instruments Triton™ 200.....	40
Figure 19. The measurement setup.....	42
Figure 20. Monitoring the bias cooling.....	45
Figure 21. Pinch-off test.....	46
Figure 22. Transport through a large quantum dot on device NO9a:.....	47
Figure 23. Setting up the compensation for SQD.....	48
Figure 24. Schematics for the reflectometry circuit.....	49
Figure 25. Measured reflected signal.....	50
Figure 26. The fabricated devices.....	52
Figure 27. An SEM picture of a device identical to the one measured in this study.....	53
Figure 28. A double dot formed in the Q1m and Q1r positions.....	54
Figure 29. The coupling between the dots and a spin blockade.....	55
Figure 30. Singlet-triplet splitting.....	56
Figure 31. Triple dot in Qubit 1 region.....	57
Figure 32. The multi-electron dot.....	58
Figure 33. Suggested geometry for further studies.....	63

## **Abstract**

For the experiments a GaAs/AlGaAs heterostructure material with a 2DEG 57 nm below the surface was chosen. A fabrication recipe was developed for the ohmic contact lithography, annealing, the production of 30 nm wide metallic depletion gates and cobalt micromagnets. The produced devices included implementation of following ideas: implementing a multi-electron quantum dot for qubit operations and coupling of the qubits, using a metallic “floating” gate for better sensing of the qubits, preparing micromagnets for easier operation of the qubits. The designed devices had opportunities for testing all the implemented ideas, performing operations on up to two triple dot qubits, one large multielectron dot and two sensor quantum dots. A special sample board was designed for this experiment. A number of fabricated devices were measured in an Oxford Instruments Triton™ 200 cryogen free dilution refrigerator at base temperature on the order of tens of mK. The presented data for the device NO9b includes transport, charge sensing, reflectometry and single shot readout measurements of the quantum dots. A double quantum dot is tuned up and brought into a spin-blocked regime, and a triple quantum dot is tuned up. The metallic floating gate did not seem to disturb the quantum dots, a design for testing the sensing capabilities is suggested. The large multi-electron dot was tuned up and showed dense Coulomb oscillations. The dot could not be operated as intended due to an inconvenient gate layout. On the basis of the measurement a better design for the multi-electron dot is suggested. The micromagnets melted during the fabrication process, a better recipe is suggested. The achieved results showed potential for the future multi qubit devices.

## **Acknowledgements**

I would like to thank Charlie Marcus for the great opportunity to work in such a well-functioning lab. Thanks for the project and all the inspirational talks and all the guidance. I would like to thank Ferdinand Kuemmeth for all the guidance with the experimental electronics. Thanks a lot to Anton Kovyakh for working together on the measurements and sharing the experiences together.

Thanks to Peter Dahl Nissen for working together on the fab recipe and help with the experiment. Thanks to Shivendra Upadhyay for all the fab guidance. Thanks to Martin Kufahl for working together on the “15 in a row” project.

I would like to thank the spin-qubit team for some general guidance in the qubit world, as well as everybody who read chapters of my thesis.

A special thank to our secretaries Jess, Katrin and Tina for all the support and making the QDev an awesome place to be and all the QDevers for the good atmosphere and QDev Ladies for all the inspirational discussions.

# Introduction

---

*The context for the development of quantum computers may be clarified by comparison to a more familiar quantum technology: the laser... Lasers do not replace light bulbs for most applications; instead, they produce a different kind of light – coherent light which is useful for thousands of applications... Likewise, a quantum computer will not necessarily be faster, bigger, or smaller than an ordinary computer. Rather, it will be a different kind of computer, engineered to control coherent quantum mechanical waves for different applications.*

*T. D. Ladd et.al. [[1]]*

The basics of a quantum computer rely on the ability of a bit of quantum information (a qubit) to be in a superposition of two states, obeying the laws of quantum mechanics. Such a system would be good for optimisation, calculation of energy states of quantum systems, such as molecules, and factorisation of numbers, useful for cryptography. This does not mean that a circuit build of qubits will be faster at performing computations available on a classical computer, it would supplement the existing computers with the new abilities.

**Table 1. Criteria for implementation of the quantum computations proposed by David P. DiVincenzo in “The Physical Implementation of Quantum Computation” from 2000 [2].**

- A scalable physical system with well characterized qubits
  - The ability to initialize the state of the qubits to a simple fiducial state, such as  $|000\dots\rangle$
  - Long relevant decoherence times, much longer than the gate operation time
  - A “universal” set of quantum gates
  - A qubit-specific measurement capability
    - The ability to interconvert stationary and flying qubits
    - The ability faithfully to transmit flying qubits between specified locations

The first idea for a qubit was proposed by S. Wiesner in 1983 [3]. Since then, many different ways of implementing a quantum bit have been demonstrated. From a quantum informational point of view, implementing a fault tolerant qubit with a mechanism of quantum error correction would require a number of physical qubits [4]. This means that implementation of a logical qubit might require fabrication and operation of a number of coupled physical qubits. This raises the question of producing a qubit that has scalability potential, rather than finding a perfect qubit that can perform all the single qubit operations with high fidelity.

A turning point in the field of spin qubits was a paper from 1997 by Daniel Loss and David DiVincenzo[5] where they proposed performing quantum computations using spin states in quantum dots. This theory kick-started the series of experiments, which successfully implemented the Loss-DiVincenzo qubit and many other types of qubits that use spin states in semiconductor quantum dots[6]. In 2000 DiVincenzo published another paper[2], where he described the criteria for a quantum computer (see Table 1). Those criteria have been partially fulfilled in different types of spin qubits.

Right now the field of the spin qubits is on the borderline towards scaling up to the multiple qubit operations. Full control of one[7], two[8] and three-electron[9, 10] qubits have been demonstrated, a two qubit gates have been performed. At this point it is important to realise what the failure modes are for the existing qubits and develop a qubit recipe that would allow easy operation and provide the best potential for the scalability.

One of the qubits with a good potential for scalability and perhaps ease of operation is a two-electron qubit, that gains one axis of control using constant magnetic field and second axis of control using a gradient magnetic field provided by a micromagnet. An electron can be brought into oscillations along the magnetic field gradient and hereby experience an oscillating magnetic field within the frame of reference of that electron. The original aim in this thesis has been designing an experiment that can implement, operate and couple two of such qubits. A layout for an experiment was designed and basic measurements characterising the system were performed.

The designed quantum dot geometry implements a number of new ideas that can improve qubit operation and sensing. For the first, “floating” metallic gates that should couple the sensor quantum dot with the qubit dots were designed. This technique would allow moving the sensing dot away from the qubit, which will make the sensor less coupled to the operation gates of the qubit that causes loss of signal, and might help sensing the qubits individually, without any noise from other surrounding qubits. For the second, a multi-electron dot was implemented into the design; the large dot can either be used as a part of a qubit, or as a mediator between the qubits. Usually the quantum dots are operated in a few-electron regime. If the same operations can be done within a many-electron regime, a lot of time for tuning the dots into a low electron regime can be saved; this adds an extra ease to the operations. Such a large quantum dot, or a long quantum channel (“sausage”) can also be useful as a mediator between the qubits, which can allow adding space between the qubits, and easier control of the coupling between the qubits.

During the fabrication, the micromagnet samples were damaged. The designed devices had many other opportunities for implementations of different types of qubits. The measurements were therefore aimed after characterising the multi-electron dot and using it for operations within a triple quantum dot. Usually triple quantum dots are used in a regime of one electron per dot with a total spin  $\frac{1}{2}$  for each of the electrons. The essential part of this new physics problem is the question of performing the same kind of operations in a system where one of the quantum dots does have multiple electrons. The interesting questions are: whether the total spin state of the multi-electron dot would remain  $\frac{1}{2}$ , how the electrons within the dot will interact and arrange themselves, and how the occupancy of such a multi electron dot would influence the performance of the three-electron qubit.

In this thesis you will read about the implementation of the described ideas including design, fabrication and measurements. In Chapter 1, the background for the ideas is described. All the practical considerations before the experiment are explained in Chapter 2. The measurement details are briefly outlined in Chapter 3 and the results of the performed measurements are presented in Chapter 4.

# Chapter 1. Background

Quantum mechanics has brought us towards better understanding of the world surrounding us. We are built of particles, which obey the laws of quantum mechanics. We can describe the movements of the bodies that consist of billions of particles, but dividing the problem up into individual particle movements and interactions within all the individual molecules is impossible to calculate using the existing computing power. The calculations on the quantum systems should therefore be executed using the quantum systems. Building a quantum computer would resolve many questions about everything that exists.

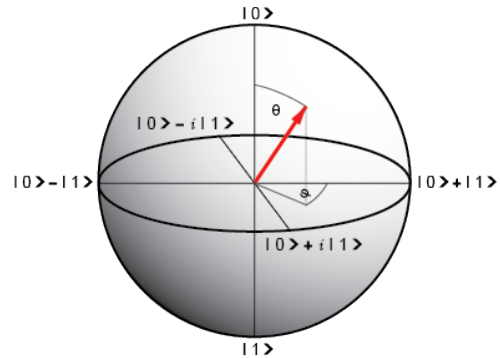


**Figure 1. The Bloch sphere.**

The sphere represents all the linear combinations of the two states in the north and south pole of the sphere. The  $\theta$  and  $\phi$  are the variables for the spherical coordinate representation of the state coefficients. The red arrow represents the state  $|\psi\rangle$ .

## 1.1 Quantum bit of information

Nowadays, information is processed using binary systems. In a classical sense, a bit of information can take a value of either 0 or 1, where each bit is a part of the unambiguously encoded system. Such systems are robust and efficient, when it comes to linear operations, however, there are types of calculations that will take millions of years to perform for a classical computer, such as calculating the energy states of molecules and several optimisation processes. A quantum computer would be a better alternative for such problems. [11]

### 1.1.1 Definition

A quantum bit of information obeys the laws of quantum mechanics as it can be in a superposition of the  $|0\rangle$  and  $|1\rangle$  states. The following linear combination can describe the state of the qubit, also expressed in terms of spherical coordinates:

$$|\psi\rangle = \alpha |0\rangle + \beta |1\rangle = \cos\left(\frac{\theta}{2}\right) |0\rangle + e^{i\phi} \sin\left(\frac{\theta}{2}\right) |1\rangle, \text{ where } |\alpha|^2 + |\beta|^2 = 1$$

Such a representation of a qubit can be mapped on a Bloch sphere [12], where all the linear combinations of  $|0\rangle$  and  $|1\rangle$  are located on the surface of the sphere. Such a sphere is shown in Figure 1. The states  $|0\rangle$  and  $|1\rangle$  can represent charge or spin states of the quantum system. A spin qubit is a system, where these ground states are represented by spins (either single, or multiple spins in one state).

### 1.1.2 Types of spin qubits [13]

The spin qubits can use different spin states as a basis. In this section, spin qubits using one and two electrons will be described. For the spin qubits operating with one electron, the two spin states for operation would be the  $|\uparrow\rangle$  and  $|\downarrow\rangle$ . Readout of a qubit with one electron requires a large Zeeman splitting. This is achieved by measuring in a high magnetic field environment. The two spins are aligned parallel to the magnetic field direction, one of the spins will be in the same direction as the magnetic field lines and the other will be in the opposite direction.

For operation of the single spin qubit, the  $\pi$ -rotations around the x- and y-axis are performed. The rotations are realised using ESR (electron spin resonance) technique, applying an AC magnetic field that drives the coherent oscillations between the  $|\uparrow\rangle$  and  $|\downarrow\rangle$  states. The direction of the oscillating magnetic field is perpendicular to the static field; the frequency is equal to the Larmor frequency:

$$\omega = \omega_L = \frac{g \mu_B B}{\hbar},$$

where B is the amplitude of the static magnetic field,  $\mu_B$  is the Bohr magneton and g is the g-factor. The coherent rotations can be performed around any vector in x-y plane, the rotation axis is determined by the phase of the oscillating field. The angular rate of the  $\pi$ -rotations is given by the Rabi-frequency:

$$\Omega = \frac{g^* \mu_B B_{AC}}{2 \hbar},$$

where  $B_{AC}$  is the amplitude of the AC-field and  $g^*$  is the effective electron g-factor. If the basis for the qubit operations consists of two electrons, the two states of operation are singlet and triplet states. In a magnetic field, the triplet state is split into 3 spin states:

$$S = \frac{|\uparrow\downarrow\rangle - |\downarrow\uparrow\rangle}{\sqrt{2}}$$

$$T_0 = \frac{|\uparrow\downarrow\rangle + |\downarrow\uparrow\rangle}{\sqrt{2}}, \quad T_+ = |\uparrow\uparrow\rangle, \quad T_- = |\downarrow\downarrow\rangle$$

The common choice for the basis is combination of the S and  $T_0$  states. The magnetic field (Zeeman splitting) makes sure that the leakage into the other triplet states is minimal. The singlet-triplet qubit can perform coherent rotations around the z-axis, using the exchange energy J (the energy difference between the two states). For the second axis of control of a singlet-triplet qubit, the local magnetic field gradient is needed, generated either by micro magnets or by the local nuclei.

## 1.2 Quantum dots and qubit implementations

### 1.2.1 Quantum dot

A system with discrete level spacing containing a controlled number of electrons is called a quantum dot (except for the superconducting and metal quantum dots). Such quantum systems are also called artificial atoms, since they have the quantized energy levels, just as atomic orbitals. The control of the number of electrons in the dot is usually performed using a metallic depletion gate, capacitively coupled to the dot. A quantum dot is coupled to the electron reservoirs via tunnel barriers. These reservoirs are attached to the outer electrodes and are called the source and the drain. By setting a certain voltage drop between source and drain electrodes, called bias voltage, the electrons can be filled in and out of the quantum dot. In Figure 2A, a schematic representation of a quantum dot is shown.

Quantum dots have been realised in very different types of systems during the past decades. Some of the most well known systems are the superconducting dots [14], metal dots [15], trapped ions [16], ferromagnetic nanoparticles [17] and semiconductor quantum dots. In this thesis the semiconductor materials are chosen for defining of the dots.

The quantum dots in semiconductor materials can be divided into two different categories: lateral and vertical. In vertical quantum dot system, the source and drain electrodes are located above and below the quantum dot. Such a system is usually realised in a one-dimensional system, which is either gated or grown in a specific way, already containing the dot region. A vertical quantum dot is therefore defined as a 1D

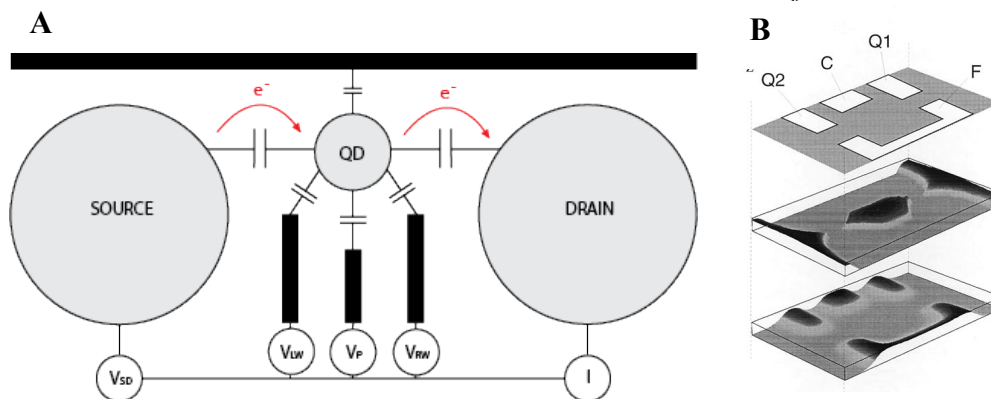


**Figure 2. Laterally defined quantum dot.**

A. The schematics of a quantum dot: the electrons can tunnel in and out of the dot. The voltage set through the gates (LW = left wall, P = plunger, RW = right wall, BB = backbone) controls electrostatics of the dot and are all coupled to the dot.  $V_{LW}$  and  $V_{RW}$  control tunnelling barriers to the source and drain electrodes.  $V_{SD}$  sets the bias voltage;  $V_P$  controls the occupancy of the dot. B. Lateral quantum dot simulation by A. Scholze et.al. [18]

system restricted to 0 dimensions. In the lateral system, a 2D electron gas is depleted by metallic gates restricting the system down to 0 dimensions. In a system like that, the quantum dot is located in the same plane as the source and drain electrodes. A schematics and simulation of a laterally defined quantum dot is shown in Figure 2A,B. The most common materials used for defining quantum dots are Silicon, Gallium or Indium Arsenides or Antimonides. The choice of material depends on the material properties and is described in Chapter 2.

### 1.2.2 Lateral quantum dots in a 2DEG

For realising a lateral quantum dot in a semiconductor material, the electrons in the material need to be restricted into two dimensions. This is achieved by iterating the material composition in the layers of the semiconductor crystal. For this thesis, GaAs/AlGaAs hetero structures are used. The GaAs crystal is grown in an MBE chamber, adding layers of AlGaAs and dopants. The wafers grown for this thesis are produced by the Manfra group from Purdue University.

The electrons in the 2DEG are depleted using metallic top gates, by applying negative voltage. The electric field lines go through the 2DEG and push away the electrons underneath the gates. The thinner the metallic gates are (width of 30-50nm), the more precise the depletion pattern. The depth (efficiency) of the depletion depends of the distance between the 2DEG and the surface of the wafer, where the gates are located.

The quantum dot region is capacitively coupled to the depletion gates surrounding the island. The total capacitance can be expressed as a sum of capacitances between each gate and the dot (as shown in Figure 2A)

$$C = C_{RW} + C_P + C_{LW} + C_{BB},$$

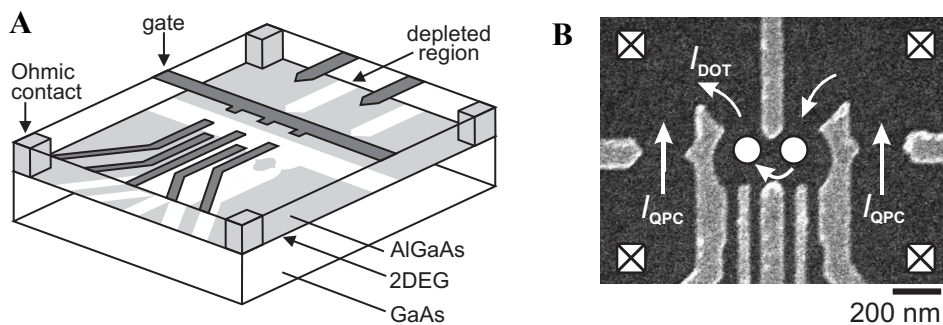


**Figure 3. Two-dimensional electron gas.**

A. The schematics for two dimensional electron gas, showing the depletion gates and ohmic contacts. B. SEM of a double quantum dot. The arrows show the current through the quantum dots and sensor quantum point contacts. White crossed-out circles show the placement of the ohmic contacts. Both figures are adapted from a review by Hanson[6]

The coupling decays with the distance between the dot and the gate. Since so many gates are involved in operation of a multiple dot system, some of the gates meant to control the qubit region can influence other dots on the device (for example the sensor dot). The principal behind operation of a quantum dot using depletion gates is illustrated on Figure 4.

### 1.2.3 Transport and sensing

The quantum dot has quantized energy levels, which means that the electrons inside the dot can only take certain energy values. The dot can be defined by those energy levels, the value of the chemical potential (that defines the highest occupied energy level) and the tunnelling barriers (that serve as barriers between the dot and the environment around it). In Figure 4A the schematic representation of a double dot system is presented, where the two dots are separated from each other by a tunnelling barrier. The environment around the dots is an energy continuum, where the electrons can tunnel in and out of the dots through the tunnelling barriers under the right conditions. The tunnelling event can occur when there is a difference in chemical potential on the left and right side of the dot (the left and right side are called source and drain and the difference in the potential is called a bias window), and a dot energy level is inside the bias window. A current of electrons can tunnel in and out of the dot, if and only if one of the energy levels is inside the bias window. There will be no current if no energy level is situated inside the bias window. This phenomenon is called the Coulomb blockade, when the current through a quantum dot is blocked due to quantization of energy levels. The Coulomb blockade can occur only if the bias window is smaller than the distance between the energy levels inside the dot. In the laterally defined quantum dots, the “wall” gates control the tunnelling barriers to the environment, the “barrier” gates control the tunnelling barriers

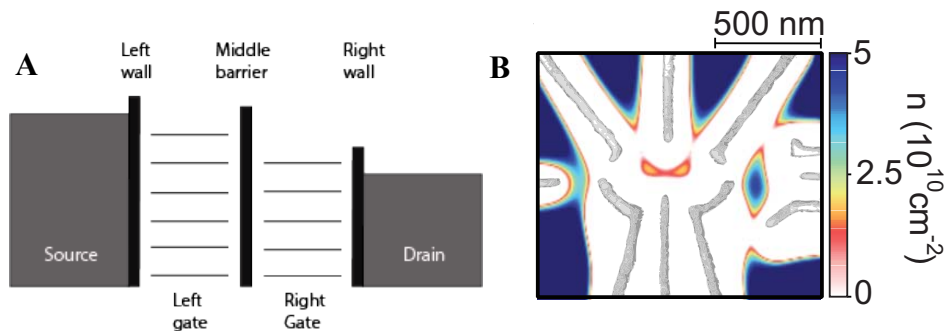


**Figure 4. Metallic gates, depletion of the 2DEG.**

A. Gate energy diagram for a double dot. Source and drain regions represent the 2DEG surrounding the double dot, are an energy continuum. Each dot has discrete level spacing. The walls represent the tunnelling barriers from the dots to the environment around the dots. The middle barrier represents the tunnelling barrier between the dots. The left and right gates control the occupancy (number of electrons) of the right and left dot respectively. Under the right circumstances a plunger gate should be able to bring the quantum dot into a zero electron regime. Plunger gates, walls and barriers are each represented by a depletion gate in a system of lateral quantum dots. B. Depletion gates in 2DEG at a negative gate voltage form quantum dots in a 2DEG. This simulation is adopted from Ref. [19]

between the quantum dots and the “plunger” gates control the chemical potential of the quantum dots. The peaks of conductance are called Coulomb oscillations, each peak represents adding an electron into the system. A schematic representation of Coulomb oscillations in a single quantum dots is presented in Figure 5A, where the voltage in the plunger gate controls the occupancy of the quantum dot.

When measuring Coulomb oscillations in a double quantum dot, a 2D graph is needed: voltages of the two plunger gates control the Coulomb oscillations, and the conductance through the dots is usually represented by a colour scale. If the two quantum dots were not coupled, the Coulomb oscillations in each quantum dot would be perpendicular to the plotted voltage axis. When the two quantum dots are dependent on each other and the plunger gate of one dot influences the other dot, the two dots are coupled. The conductance plot for two coupled quantum dots looks like the schematics in Figure 5B. The relationship between the conductance and the plunger gate voltages is called a charge stability diagram. Charge stability diagrams have recently been obtained up to a quadruple quantum dot system.[20]

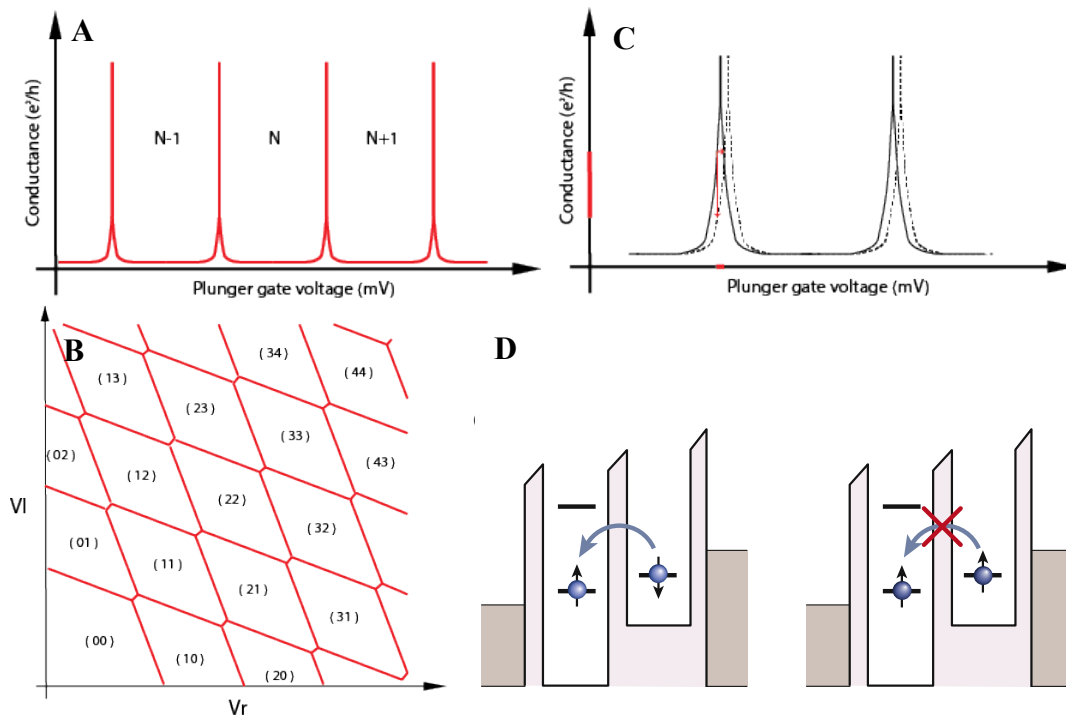


**Figure 5. Coulomb and spin blockade.**

A. Coulomb oscillations in one quantum dot. Every time an energy level in the quantum dot aligns with the bias window a current can run through the dot. B. Coulomb oscillations in two quantum dots. The two quantum dots are coupled, therefore the slope of the Coulomb oscillations show the dependency of the Coulomb oscillations on both the right and the left plunger. C. An illustration of a charge sensor: every time the electrostatic environment near the dot changes, the Coulomb peaks slightly move along the voltage axis. A small change in the Coulomb peak position will show a large change in the conductance through the sensor quantum dot. D. Pauli blockade: due to the Pauli principle two electrons with the same spin state can not occupy the same energy level. The electron transport can therefore be blocked until the spin in the blocked energy level flips. The figure adapted from Ref. [21].

In practice, the transport through an array of quantum dots can stop before emptying all the dots for electrons. In that case, the charge stability diagram can be obtained with a help of a sensor dot. The sensor dot is placed close to the measured quantum dots, such that any change in the electrostatic potential of the quantum dots would slightly change the potential of the sensor dot. The sensor dot is then “parked” on a slope of a Coulomb oscillation. The slight changes in the electrostatic potential in the sensor dot would shift the Coulomb oscillations, which would give a large change in the conductance through the sensor dot. The principal is illustrated in Figure 5C.

#### 1.2.4 Pauli blockade

Pauli exclusion principal states that two particles with the same quantum numbers cannot occupy the same quantum state simultaneously. Due to this principal, the transport through a double dot system can be blocked, if this rule cannot be fulfilled. In Figure 5D the schematics of the principal is shown for a double dot. The same principal applies for any two dots in a multi dot system.

#### 1.2.5 Improving capacitive coupling to the sensor

The sensor quantum dot is capacitively coupled to the qubit region, which allows sensing of the electrostatic environment in the qubit. In order to increase the sensitivity, a metallic gate can be placed between the sensor dot and one of the dots in the qubit. The gate would not be connected to a grounded contact, if any charges were trapped on the gate, there would not be a possibility to remove those charges. The metallic gate is in a sense “floating”, as it is not connected to anything. Supposedly the floating metal gate should increase the coupling between the sensor dot and the qubit dot and hereby improve the sensing signal.

Such a floating metal gate was suggested by Luka Trifunovic *et. al.* [22] for long-distance coupling between qubits. The “dogbone” metallic gate has never been used for coupling sensor dot with the qubit. A suggested geometry for such floating gate is shown in Figure 11. The gate should increase the sensitivity, even though the sensor is located far away. The discussion of the geometries is continued in Section 2.1.

#### 1.2.6 Realisation of spin qubits in lateral quantum dots

The mentioned single and double electron spin qubits are realisable in 2DEG lateral quantum dots. The one-electron spin qubit is better known as the Loss-DiVincenzo qubit, was proposed by Daniel Loss and David DiVincenzo in 1998 [5]. A spin qubit containing two electrons is known as a singlet-triplet qubit has been realised in many different materials end geometries as well. There are studies suggesting that birds use a similar mechanism of singlet-triplet transitions for navigation, using magnetically sensitive chemical reactions in molecule radical pairs, but unlike the experiments described in this thesis, at room temperature. [23]. The only challenge for both singlet triplet qubits and

Loss-DiVincenzo is obtaining the second axis of control, which requires an oscillating magnetic field.

#### 1.2.6 $\pi$ -rotations using micromagnets

The second axis of control for singlet-triplet qubits has been realised using gradient in nuclear magnetic fields [24], magnetic resonance in oscillating magnetic field (electron-spin resonance, ESR)[25], and by applying micro magnets close to the operating qubits both in lateral and vertical systems [26, 27]. The oscillating magnetic field can efficiently drive rotations around the Bloch sphere; however, the high frequency magnetic field heats up the electrons and is hard to operate.

While applying a static magnetic field gradient along the quantum dots, the electrons can be brought into oscillations along the field. In the coordinate system of the electron, the magnetic field would be oscillating, and would drive rotations around the Bloch sphere, using the same principle as ESR.

Many experiments within this field using GaAs heterostructures have been done in the Seigo Tarucha group at the university of Tokyo. The qubit operations using micromagnets have been shown for single-electron operations in single quantum dot [26, 28], single spins in double quantum dots [29, 30]. In silicon-based heterostructure with a use of accumulation gates two axis of control were realised in a singlet-triplet qubit [31].

An interesting experiment would be to design a system with two qubits, each with qubit state that is driven around the z-axis using the Zeeman splitting and the exchange interaction and around a vector in x-y plane using an oscillating magnetic field. The oscillating field is thought to be created by a micromagnet that creates a gradient in magnetic field between two quantum dots. By pulsing an electron between those quantum dots, the electron, from its own coordinate system, would experience oscillating magnetic field.

### 1.4 Qubits in three quantum dots

One axis of control for the described qubits can be achieved by the exchange splitting due to a large static magnetic field. The second axis of control can be achieved by an oscillating magnetic field, or a micromagnet, as described in the previous section. Another powerful and solid method for operating a quantum dot spin qubit is adding a third dot to the system. In this case, the rotations around two different axis can be achieved purely by electrical signals.

#### 1.4.1 Resonant exchange qubit

Resonant exchange qubit is realised in a triple quantum dot, using 3 electrons. The plunger gates control the occupancies of each quantum dot and the barriers control the

tunnelling barriers for each dot. Once the three dots are tuned into a symmetrical (111) regime, where there is one electron in each dot, the tunnelling barriers are kept constant, while the plunger gates control the qubit. The size of (111) region is controlled by the middle plunger gate (the gate voltage determines the position of the middle dot transition line, by changing the gate voltage, the transition moves diagonally on the charge stability diagram). The detuning, the distance from the middle of (111) region, is controlled by the left and right plungers. A schematic for a charge stability diagram in a triple dot is shown in Figure 6A. In principal, a triple dot should be represented by a 3-dimensional diagram, since there are 3 plunger gates that control the Coulomb oscillations, however a 3 dimensional plot would be hard to analyse. Instead, a 2-dimensional slice through the 3D qubit space is used for analysis of the triple quantum dots.

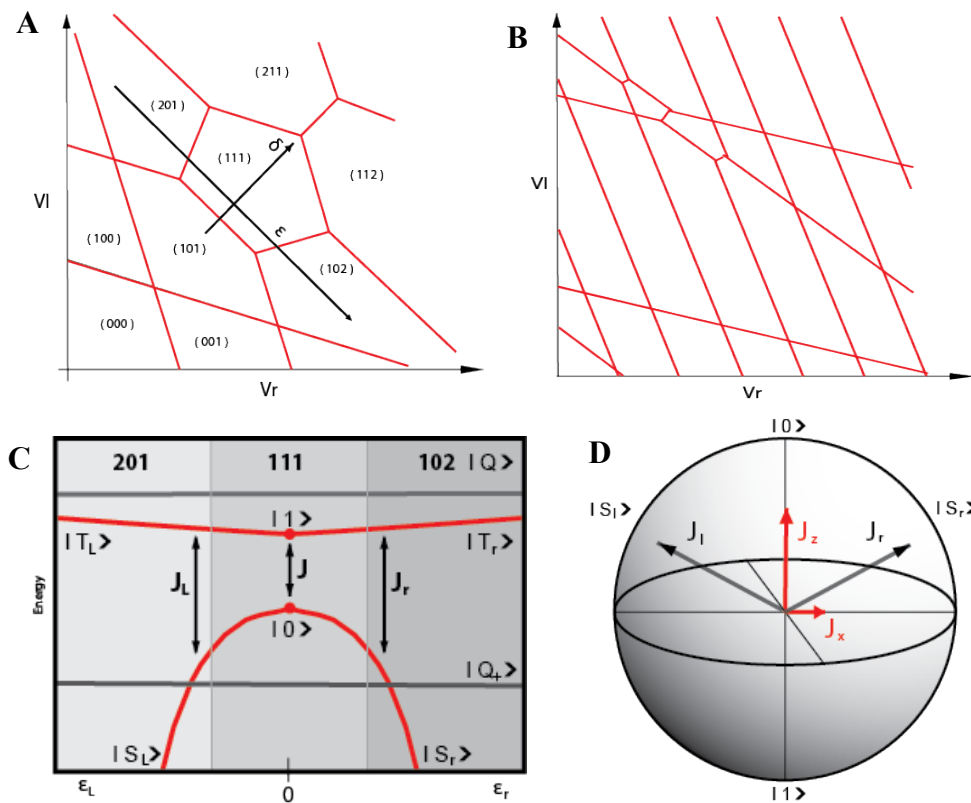


**Figure 6. Triple quantum dots.**

A. Coulomb oscillations in three quantum dots. There are three slopes in the charge stability diagram corresponding to 3 quantum dots with Coulomb oscillations in each of them. The quantum dots are obviously coupled, it can be seen out of the slopes of the Coulomb oscillations. B. Charge stability diagram for a triple dot with one asymmetrically large dot. The right quantum dot has more frequent Coulomb oscillations, which means that the quantum dot is much larger than the other two quantum dots and that it has many more electrons in it. C. Energy diagram for the operation states for the triple dot. The red curves are used for operation of the qubit. The black energy states are the leakage states and need to be avoided. D. Triple dot states mapped on the Bloch sphere.  $J_L$  and  $J_r$  are separated  $120^\circ$  from each other.  $J_z$  is the sum of  $J_L$  and  $J_r$ .

The basic configuration for a resonant exchange qubit consists of 3 electrons: there are 8 possible states for combinations of those, the following 4 states are important for the qubit operations:

$$\begin{aligned}
|0\rangle &= \frac{|\uparrow\uparrow\downarrow\rangle + |\downarrow\uparrow\uparrow\rangle - 2|\uparrow\downarrow\uparrow\rangle}{\sqrt{6}} \\
|1\rangle &= \frac{|\uparrow\uparrow\downarrow\rangle - |\downarrow\uparrow\uparrow\rangle}{\sqrt{2}} \\
|Q_+\rangle &= |\uparrow\uparrow\uparrow\rangle \\
|Q\rangle &= \frac{|\uparrow\uparrow\downarrow\rangle + |\uparrow\downarrow\uparrow\rangle + |\downarrow\uparrow\uparrow\rangle}{\sqrt{6}}
\end{aligned}$$

The  $|0\rangle$  and  $|1\rangle$  states are chosen as basis for the electron wavefunction  $|\psi\rangle$ . The states  $|Q_+\rangle$  and  $|Q\rangle$  are the potential leakage states, since the energy for those states is close to the energy of the  $|0\rangle$  and  $|1\rangle$  states. The diabatic passage through the energy diagram ensures that the

On the charge stability diagram for the triple dot in Figure 6A, the detuning axis  $\varepsilon = (V_l - V_r)/2$  and the common voltage axis  $\delta = (V_l + V_r)/2$  are designated. In Figure 6C, the detuning parameter is plotted against the energy of the described states in the (111) region. When following the detuning axis  $\varepsilon$  into the (201) region, the  $|0\rangle$  and  $|1\rangle$  states change into  $|S_l\rangle$  and  $|T_l\rangle$  states respectively. When following the detuning axis  $\varepsilon$  into the (102) region, the  $|0\rangle$  and  $|1\rangle$  states change into  $|S_r\rangle$  and  $|T_r\rangle$  states respectively. The “singlet” and “triplet” states have the following configuration:

$$\begin{aligned}
|S_l\rangle &= \frac{|\uparrow\downarrow\uparrow\rangle - |\downarrow\uparrow\uparrow\rangle}{\sqrt{2}} \\
|S_r\rangle &= \frac{|\uparrow\uparrow\downarrow\rangle - |\uparrow\downarrow\uparrow\rangle}{\sqrt{2}} \\
|T_l\rangle &= \frac{|\downarrow\uparrow\uparrow\rangle + |\uparrow\downarrow\uparrow\rangle - 2|\uparrow\uparrow\downarrow\rangle}{\sqrt{6}} \\
|T_r\rangle &= \frac{|\uparrow\uparrow\downarrow\rangle + |\uparrow\downarrow\uparrow\rangle - 2|\downarrow\uparrow\uparrow\rangle}{\sqrt{6}}
\end{aligned}$$

The singlet and triplet states have got the name due to a created “singlet” and “triplet” states in the right or left pair of electrons in the triple dot. The exchange energy  $J$ , the energy difference between the two operation states is smallest at  $\varepsilon=0$  and as seen from the energy diagram increases at  $\varepsilon<0$  and  $\varepsilon>0$ . The mapping of the presented states on a Bloch sphere is shown in Figure 6D.

If the system is completely symmetrical, the same manipulations can be done on both sides of (111) region. This requires a completely symmetrical (111) region. For initialisation and readout, both sides need to be in spin blockade. The spin-blocked area on the charge stability diagram would serve as a readout point. If the electron in the end of manipulations was in  $|0\rangle$  state, passing into the (201) region would bring the state into  $|S_l\rangle$ , which is already a ground state. If the electron in the end of manipulations was in  $|1\rangle$  state, passing into the (201) region would require the electrons to go into  $|T_l\rangle$  state, the triplet, that is prohibited to move into the 201 area by spin blockade. The triplet has a relaxation time in the order of microseconds, this allows to readout the percentage amount of singlet and triplets as a statistics of a number of such events. The readout is executed using the spin-blocked area on the charge stability diagram via comparison of the conductance on the (111), (201) and spin-blocked area that has a mixed value, due to some of the triplet states being trapped in the (111) region.

The qubit rotations are performed using diabatic and adiabatic pulsing along the detuning axis between (201), (111) and (102) regions on the charge stability diagram, as well as other charge states for initialisation. Depending on the rotation frequency and axis, different types of pulse sequences are used for moving around on the energy diagram in Figure 6C, using exchange energy  $J_z = (J_L + J_r)$  as Zeeman energy instead of the Zeeman splitting with a magnetic field. An experiment using one axis of control for exchange only qubit has been done by Laird *et. al.*[32], two axis of control were achieved by Jim Medford *et.al.* [9]for the resonant exchange qubit.

#### 1.4.2 Asymmetric system with a multi level dot

The resonant exchange qubit is both thought and implemented as a qubit that uses purely three quantum dots with three electrons for operations. The question of how the spins would interact if one of these quantum dots would contain an odd number of electrons larger than 1 is yet unresolved.

Two axes of rotation have been achieved in a triple dot with the symmetrical couplings on the right and the left side. Now, if one of the quantum dots was a large multi-level quantum dot with frequent Coulomb oscillations and random occupancy, as shown in Figure 6B, where the right dot is obviously larger than the left and middle dots, would the occupancy of the large dot control the rotations in the double dot just as in the resonant exchange qubit? The occupation of the multi-electron dot can be completely random, the assumption for the operation of such a qubit would be: if there is even number of electrons in each of the quantum dots in the “house” region, the two dots in the right and middle position should perform rotations around the Bloch sphere as in singlet-triplet qubit. If the number of electrons in the left dot is even, the quantum state composition would not match the states described in the previous section and no rotations would be possible in this regime, as illustrated in Figure 7A,B (A for working qubit and B for not working qubit). The biggest assumption here is that a large quantum dot with  $(2N+1)$

electrons in it is situated in a spin  $\frac{1}{2}$  state, which might not be entirely truth. A paper by P.W.Brouwer *et.al.* [33] suggests that the probability for spin  $\frac{1}{2}$  in an odd occupancy and probability of spin 0 for an even occupancy in a quantum dot is determined by the interaction parameter:

$$\lambda = \frac{u}{\Delta},$$

where  $u$  is the on-site Coulomb repulsion between the electrons and  $\Delta$  is the level spacing between the eigenvalues in a Hermitian random matrix representing the energy states of the system.

In Figure 7C and Figure 7D the probabilities for being in a certain spin-state are shown depending on the interaction parameter  $\lambda$ . The red and black lines represent the probability for the spin states for  $(2N+1)$  and the spin states  $2N$  respectively. For the semiconductor structures in the magnetic field the time-reversal symmetry is broken, hence the probabilities for a given spin-state are shown in Figure 7D. If the level spacing for the quantum dot is much larger then the Coulomb repulsion between the electrons, as it is for a small quantum dot, the parameter  $\lambda$  will take a low value and the probability for spin  $\frac{1}{2}/0$  for odd/even occupancy will be 100%. For the larger dots, the value of the  $\lambda$  parameter is not obvious and will depend on the local level spacing and the electron-

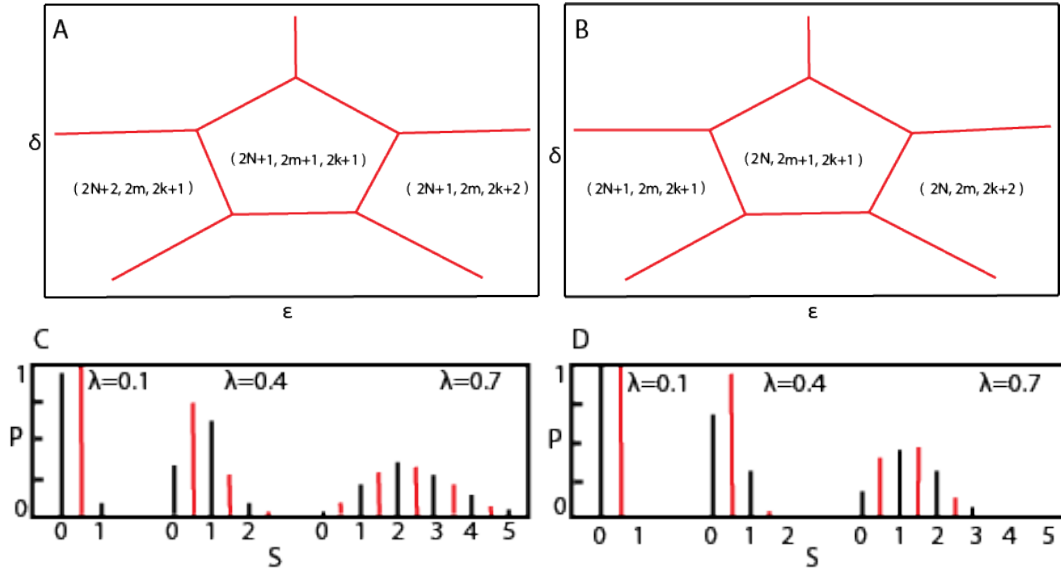


**Figure 7. Asymmetrical triple dot with a multi-electron dot in the left dot position.**

A. The “house” region with random odd/odd/odd occupancy, the  $(2N+1)$  electrons indicates a large number of electrons in the dot. Even though the triple dot is not situated in  $(111)$  region, operations on the  $\epsilon_r$  side of the qubit should be possible, assuming that the total spin state of the system is  $\frac{1}{2}$ . B. The “house” region with even/odd/odd occupancy. Supposedly this region should not be suitable for the operation of the qubit, given the multi-electron dot is in a spin-less state occupation. C,D. Probability for spin state at the different values of interaction parameter  $\lambda$ : C. for the presence of time-reversal symmetry, D. for the absence of time-reversal symmetry. Figure C,D is a re-coloured figure from the ref. [33]

electron interaction within the quantum dot. For  $u=\Delta$  the electrons would tend to space out and occupy all the possible energy levels, leaving only one electron in each level with the spins aligned in the same direction. This phenomenon is called Stoner instability.

It is completely unknown, whether the spin-states of multi-electron dots will follow the rule of spin  $\frac{1}{2}$  for odd and zero spin for even number of electrons in the quantum dot and how the electrons will influence the qubit manipulations. An experiment using a multi-electron quantum dot might not only ease the process of the tuning the quantum dots by letting operations in many-electron regimes, but also describe new physics of the electron-electron interactions within multi-electron qubits, which is a very non-trivial question.

#### 1.4.3 Multi-electron dot as a "coupler" to the next systems

An idea for a multi-electron quantum dot was first mentioned in a footnote to the original Loss-DiVincenzo article [5]. The large electron container can be a part of a qubit, as well as a coupler for two separate qubits together. A large multi electron dot between two operating qubits would serve as a mediator for the operations, not actually attending in the qubit operations, but delivering the information between the two qubits, turning the exchange between the qubits on and off. Suggestions for such experiment are described in an article by V. Srinivasa *et. al.* [34].

## Chapter 2. Preparations for the experiment

---

A spin qubit experiment does not just consist of coherent rotations around the Bloch sphere. Such an experiment requires a lot of preparations, several months of work before even getting to the measurement stage. In this chapter you will experience a complete way from getting an idea for an experiment, to setting up the measurements.

To start with, the device design of the experiment has to be thought through, taken into account the previous work and adding new innovative ideas. Then the whole procedure of fabricating the semiconductor devices has to be tested. The next stage: testing the available electronics and setting up for measurements, to know, what procedures are possible, given the conditions. Then the device design is revised, according to the restrictions of the fab and measurement apparatus.

The process of fabrication on GaAs heterostructures is a well-known and well-described process, developed by generations of experimental physicists. Even though there are many working fabrication recipes, they need to be adapted and re-adjusted every time a new machine and a new wafer are used. The prototype for fabrication procedure used in this thesis was developed by Christian Bartel[13] and Jim Medford[12] at Harvard University, however a big effort was put into developing a new working recipe for the equipment and the new GaAs material since the lab has moved to the University of Copenhagen. The development of the recipe presented in this thesis was done in collaboration with the Spin Qubit team at the Center for Quantum Devices. The description of the important experiences is provided in section 2.2, the complete working recipe can be found in Appendix A.

The measurement setup used for this thesis was developed by Jim Medford and assembled by Johannes Beil and Tomohiro Otsuka and adapted for the pioneering multi qubit experiments. The setup was almost unchanged for the experiments in this thesis the description is presented in the Section 2.6. For more details, advice Johannes Beil's or Jim Medford's thesis. The cryogenic equipment used for cooling down the sample is described in Section 2.5 and the circuit boards that are connecting the fabricated chip with the acquisition setup are described in Section 2.4.

### 2.1 Designing the pattern for the depletion gates

A common definition of a quantum dot is a zero-dimensional system with discrete level spacing, with exception of superconducting and metal quantum dots. There are many ways to realise a quantum dot in semiconductor materials, the two main approaches are the lateral and the vertical. One of the ways is to define a one-dimensional system, where

the electrons will be restricted to move along one dimension. The electrons can be restricted further by applying metallic gates across the “wire”, which will define zero-dimensional islands with controlled number of electrons [35]. Another way of making a zero dimensional system is to use a two-dimensional electron gas in a semiconductor and define dots via depletion gates. This thesis is focused on gate patterning of 2 DEGs in GaAs hetero structures.

### 2.1.1 Wafers and their crystal structure

Both GaAs and AlGaAs have a zinc blende crystal structure and the lattice constant of both crystals is identical. Due to the different band gap<sup>1</sup>, the 2DEG can be formed using doping when bringing the semiconductor structure into the low temperature regime. Properties of the 2DEG and the behaviour of the formed quantum dots are linked to the material properties of the semiconductor structure. The important properties are the g-factor of the semiconductor crystal, the spin-orbit coupling and thereby the orientation of the dots with respect to the crystal lattice,

G-factor is the material property, linked to the magnetic moment and gyromagnetic ratio of the nuclei. The effective g-factor of the nuclei is a dimensionless property, that relates the magnetic moment of the nuclear spin  $\mu$  to the spin angular momentum  $I$ :

$$\mu = \frac{g \mu_N}{\hbar} I,$$

where  $\mu_N$  is the nuclear magneton. Even though materials like InAs and InSb sound more promising in terms of G-factor, GaAs is a safe choice that is well studied, proven to be stable in terms of forming quantum dots and is easy to work with.

Spin-orbit coupling arises from the spin-orbit interaction of the electrons with the nuclei. There are two types of spin-orbit coupling: Rashba and Dresselhaus. The Rashba term comes from spin-induced asymmetry in the crystal lattice and the Dresselhaus term comes from structural inversion asymmetry. The Hamiltonian for the spin-orbit interaction in GaAs 2DEG is [36]:

$$H_{SO} = \alpha(p_x \sigma_y - p_y \sigma_x) + \beta(-p_x \sigma_x + p_y \sigma_y),$$

where  $\alpha$  is the Rashba spin-orbit coefficient,  $\beta$  is Dresselhaus spin-orbit coefficient,  $p_x$  and  $p_y$  are the momentum operators and  $\sigma_x$  and  $\sigma_y$  are the spin operators in {100} and {010} crystal orientations. The spin-orbit interaction depends on the orientation of the crystal axes with respect to the qubit axes, which means that the orientation of the sample

---

<sup>1</sup> The band gap is 1,42eV for GaAs and 2,16eV for AlAs, The AlGaAs band gap depends on the Al/Ga ratio

on the wafer must be thought through before fabrication of the devices. In our case the qubits (axis along the triple dots) were oriented along the  $\{110\}$  direction.

GaAs heterostructures are an evident choice for the 2DEG devices, though a little production property is important to note. The wafers are usually grown in smaller pieces 3-5 inches in diameter. The distribution of the dopants can change along the edges of the wafer. This means that the given mobility is only valid in the middle of the wafer and can vary out to the edges. When choosing a piece of wafer for fabrication of the samples, the location of the device on the wafer is important (along with the orientation on the crystal axis).

### 2.1.2 Evolution of the depletion gates geometries

An optimal gate layout is a key to a successful experiment. The distance between gates must be long enough, so there is a possibility to form a quantum dot. At the same time, the distance must be small enough for the dot to be able to go down to zero electrons.

An optimal layout must contain as few depletion gates per dot, as possible, to decrease the number of degrees of freedom in the system. At the same time, each dot needs a barrier, that separates the dot from the surroundings and individual plunger gate, which can control the occupancy of the dot. In Figure 8 the different suggestions for the quantum dot geometries are presented. Most of the shown devices were never even measured because of the unrealistic depletion gate layout.

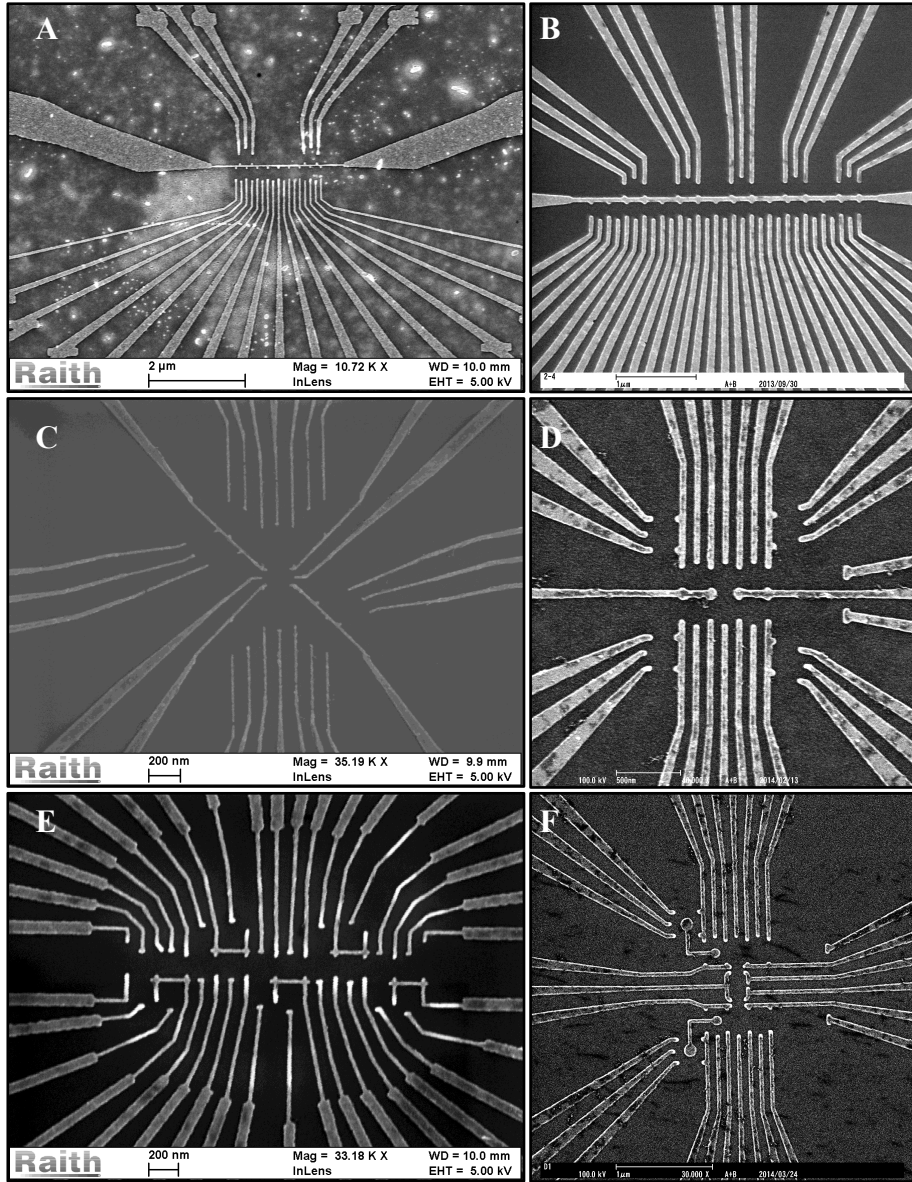


**Figure 8. SEM images, evolution of the gate designs over time.**

A. 8 quantum dots in a row. This design was expanded to 15 dots in a row, which can be seen to the right. B. 15 quantum dots in a row, this geometry was developed for operations with 5 triple dot qubits. Device NO7a, lithographically identical to the one in the figure, was measured by Martin Kufahl and Peter Dahl Nissen [37]. All the quantum dots could be tuned up one by one, and as double or triple dots. Tuning three triple dots in a row was impossible in this type of devices, since the middle triple dot did not have a place to load and unload electrons. This geometry was revised for 3 triple dots in one line, each mediated by a large multi-electron dot. This type of devices was measured by Johannes Beil and Anton Kovyakh [38]. C. Two triple quantum dots, coupled via the middle dot. The triangular outline for the triple dots might not be suitable for two-axis control, as shown in article by Laird *et.al.* [32]. This geometry was discarded. D. The linear design for the triple dots was chosen instead of the “triangular” design in the previous image. The two triple dots are situated directly behind the back bone gates, which means nothing can control the capacitive coupling between the dots. This design was extended for the final devices used for this thesis shown on fig.F. E. A design that is supposed to implement opportunities for both loss di Vincenzo, singlet-triplet, and exchange only qubits with a new sensor geometry. Those devices were never measured, since the requirement for a separate barrier between each dot and a plunger gate for control of each quantum dot was not fully met in this device. F. This design was used for the fabricated devices presented in this thesis.

## 2.2 Fabrication on GaAs/AlGaAs heterostructures

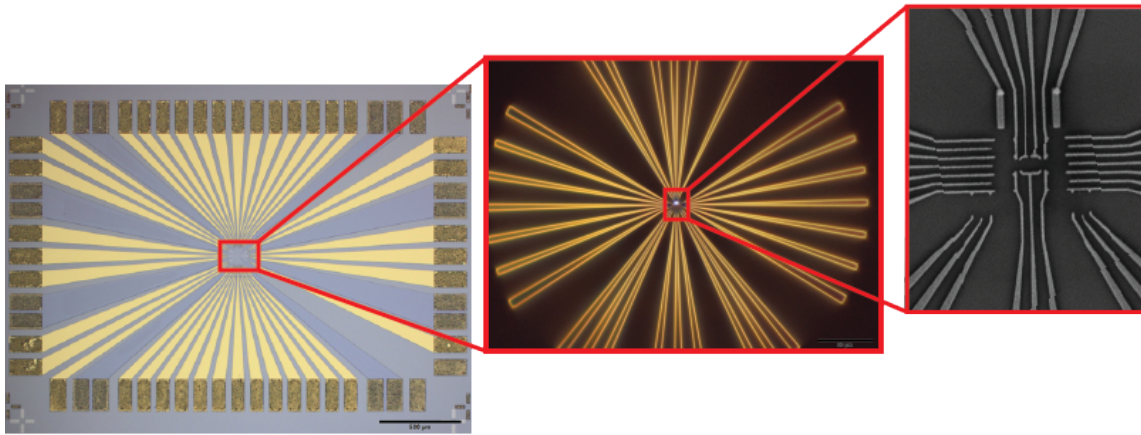


**Figure 9. A complete fabricated device.**

The device consists of an etched out mesa, annealed ohmics, fine depletion gates and the large connection gates (in this case also micromagnets). A fully fabricated device is shown in the figure, the scale of the fully fabricated device is 2x3 mm, the rightmost SEM image shows the fine gates pattern, where the distances are on the scale of hundreds of nanometers.

To start with, the two-dimensional electron gas needs to be patterned, creating separate channels, where the current will run through. The excessing 2DEG is etched away, leaving only the needed “mesa” pattern. Creating such a pattern will isolate the devices on the same chip from each other. An example of a mesa pattern is shown in Figure 11. The quantum dots will be formed in the middle of the mesa, where all the channels meet.

The 2DEG is located 50-100 nm below the surface and is impossible to contact directly. The created mesa channels are brought into contact with the outside world using the so-called ohmic contacts. A pattern, indicating the location of the ohmic contacts is shown in Figure 11. The ohmic pattern is filled with a stack of different metals. The deposited metal layers are heated up to a high temperature, so they create an alloy and make spikes through the GaAs crystal, contacting the 2DEG.

Now after getting into the contact with the 2DEG, the designed gate pattern can be fabricated. The gates are deposited in two steps. First, the finest pattern is made with a thinner layer of gold. Then a thicker layer of gold is used for larger parts of the pattern. A detailed description of the fabrication process is presented in the following sections.

A complete working recipe for the two available lithography systems was developed for fabrication of the spin qubit devices using different techniques. The detailed recipe is presented in Appendix A. In this section, the experiences, problems and solutions of the fabrication issues are presented.

### 2.2.1 Mesa patterning

There are two ways of creating a mesa pattern: dry and wet etch. In the first case, the semiconductor crystal is mechanically etched by shooting ions towards its surface. In the second case, the wafer is chemically etched with a mixture of different acids. Wet etch was used for the devices presented in this thesis.

The process of etching out a mesa consists of the following steps. To start with, the wafer is uniformly covered with photoresist (a polymer compound, sensitive to the UV light) and heated up to evaporate the solvent. Then the chip is exposed to the UV light through a patterned mask. The UV exposed resist is then developed and only the mesa pattern remains protected by the resist. The chip is then brought into an acidic solution for etching out all the excess 2DEG. The depth of the etching depends on the depth of the 2DEG and can be controlled by the etching time and the acidity of the etchant. The etching should be at least 10-20% deeper than the distance between the 2DEG and the surface to make sure that there is no 2DEG between the ohmic channels and between the devices on the same chip.

The mesa patterning part could be done with the e-beam lithography. However, e-beam resist has a different etching rate than the photoresist, which leads to an uneven etch on the edges of the mesa. This method can be improved, however the photolithography method was chosen for the devices produced for this study.

### 2.2.2 Ohmic contacts

Fabrication of the ohmic contacts is executed in 3 steps. First the lithography step, where the pattern is created, then depositing metal layers and at last the annealing step. Ohmic pattern consists of large shapes (larger than 10  $\mu\text{m}$ ), suitable for photolithography. However, the alignment in a mask aligner is always a tricky step and for the sake of convenience, the ohmic pattern is done using the e-beam lithography. Pads on the ohmic pattern are distributed over all gates, but only the pads that are distributed on the mesa channels will make contact to the 2DEG after annealing.

The principle behind the e-beam lithography is similar to the photolithography. The long polymer chains of the resist are broken by the e-beam according to the given pattern. Then the broken polymer is washed away by the developer, such that only the needed pattern is not protected by the resist. Next, the whole sample is ashed by the oxygen plasma, this procedure should remove the remains of exposed resist, to rinse the surface, where the metal stack will be deposited immediately after the ashing procedure.

The overall thickness of the resist must be larger than of the metal stack, otherwise the metals will form a uniform layer that can not be lifted off. A double layer of the resist is used for the E-beam lithography: 300 nm 9% Co-Polymer in Ethyl Lactate (EL9), 200 nm 4% PMMA in anisole (A4). EL9 and A4 have different development rates, which creates

an undercut, leading to easier lift-off. In Figure 10, the process E-beam lithography is sketched.

The quality of the ohmic contact depends on the metal stack composition and the annealing procedure. The lower contact resistance, the better quality of the contact. Different parameters have been fine tuned for this process. Different composition and thickness of metals have been tried out, the same annealing recipe works for both GePtAu and GeNiAu ohmic contacts. NiGeAuNiAu contacts have shown the most stable and reliable performance; together with a suitable annealing procedure those contacts have the lowest contact resistance.

For depositing metals two different techniques are tried out: thermal evaporation and e-gun chamber. In the first case, the material is heated up in a metallic boat until it starts melting and evaporating. The sample is placed facing the material, such that the metal particle vapour creates a smooth layer on the surface of the sample. In the e-gun chamber a stream of electrons is sent to the surface of the given material and shoots off metallic particles, which are then headed towards the sample. Both methods require high vacuum and both methods are suitable for creating a controllable thickness of the metal layer.

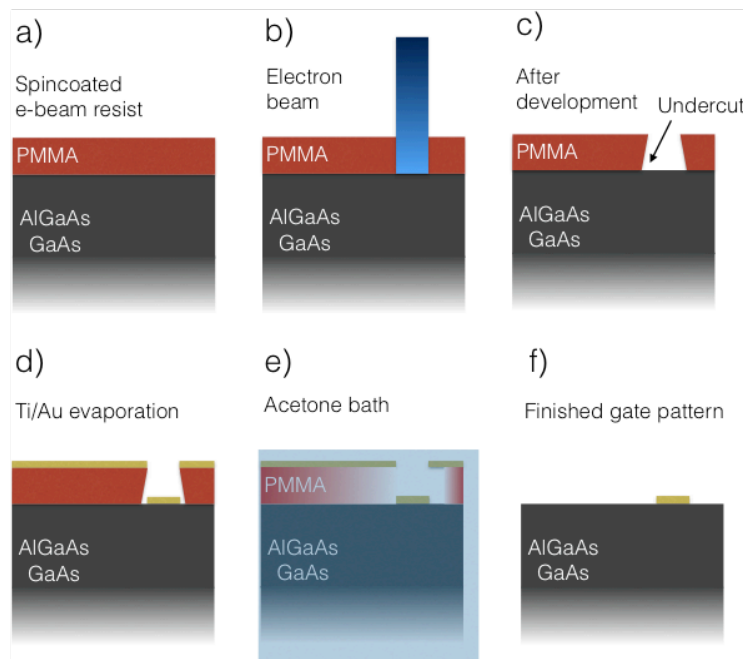


**Figure 10. E-beam lithography.**

A. The device is coated with e-beam resist. B. The resist is exposed by the e-beam using a given dose. C. The resist is developed, there is an undercut in the resist which will help the lift-off process. D. The metals are deposited onto the surface of the wafer. Usually the wafer is cleaned with oxygen plasma to remove the residues of the resist for a smoother surface. E. The chip is brought into acetone, all the resist is dissolved, all the unwanted metal lifted off the surface. F. The fabricated pattern is ready. Figure adopted from Johannes Beil's thesis [38].

The main parameters in the annealing procedure are the highest temperature and the time this temperature is held constant. In Table 2 the variety of different temperatures and different annealing times is shown. According to the results from the table, 425°C was the most optimal annealing time. Very small changes in the temperature (5 – 10 ° C) have shown a drastic improvement in the ohmic contact resistance. A detailed recipe for annealing procedure can be found in Appendix A

**Table 2. Dependence of the ohmic resistance on the annealing temperature.**

**The device NO5g-l were cleaved into 2 pieces and separately deposited 43nm Ge, 30nm Pt, 87 nm Au (cleaned with Ar plasma before depositing the ohmic contacts). Each device was annealed with different temperature, the results from the 2 batches are presented in the table. The chosen annealing recipe is presented in the Appendix A.**

Annealing temperature	Annealing time	Ohmic contact resistance
400° C	2 min	350-450 Ω
425° C	2 min	100-180 Ω
450° C	2 min	100-300 Ω
415° C	2 min	1500-2500 Ω
425° C	2 min	70-190 Ω
435° C	2 min	800-900 Ω

The resistance of ohmic contacts is measured using 4K probe station, where the contacts can be probed individually. For measuring the ohmic resistance of the contacts, the voltage is applied between the two pads on the same mesa channel and the current is measured. In this case, the resistance of the 2DEG is negligible. If measuring between the contacts on two different ohmic channels, the resistance is increased due to the added 2DEG resistance. The ohmic contacts are expected to obey Ohms law within the range of operation, if any other behaviour is observed, the contacts are not useable.

### 2.2.3 Fine gates

Fine gates patterning is a fragile step of fabrication and a lot of effort is put into improving the yield of this procedure. The fine gates pattern is written using the e-beam lithography. There are two e-beam lithography systems available at QDev: Elionix and Raith E-line, both systems are suitable for the fine gates patterning. The results are though more reproducible on the Elionix system (resipes for both systems are presented in Appendix A).

The fine gates control the size and the number of electrons in the dot. If the fine gates are too far apart, the dot will never be able to go into a zero electron regime. The width and distance between gates are therefore important parameters in this fabrication step. There are certain limitations to the minimum width of the gates. For the first, the finest feature

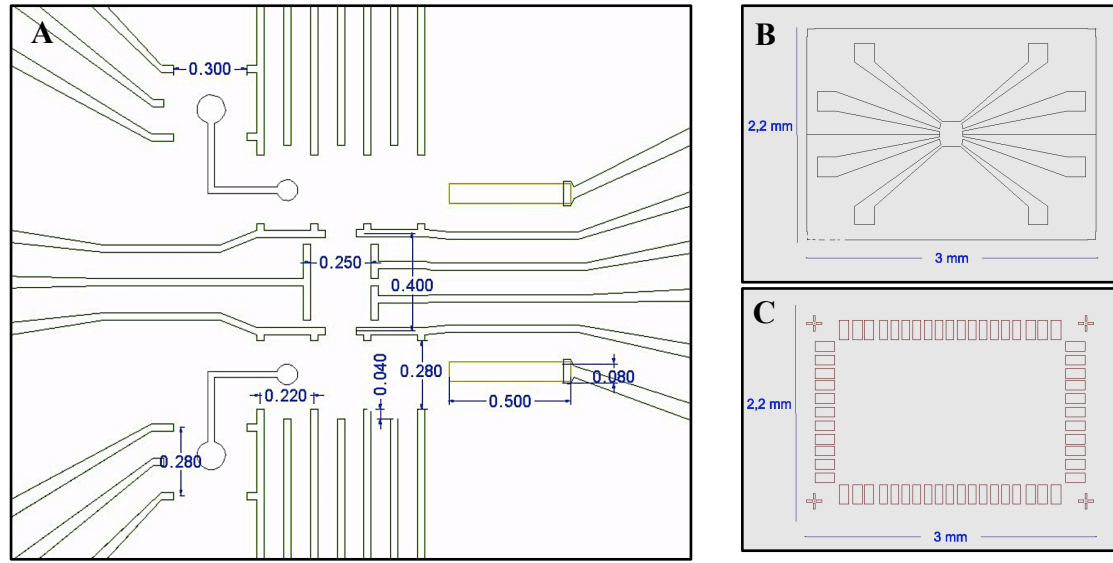


**Figure 11. The design for fabrication process.**

A. In this figure design of depletion gates for sample NO10 including the micromagnets, the large multi-electron quantum dot mediating the two triple dots and the “coupler” connecting the qubits with two charge sensors. B. Design for mesa pattern. C. Design for Ohmic contacts.

possible with e-beam lithography is simply limited by the size of the beam. For the second, the thickness of the resist both limits the thickness and the pitch: if the written gate lines are much thinner than the resist layer, the Van der Waals forces will bring the channel walls together, causing shorts in the produced gates. The same applies to the too short a distance between the lines. In Figure 12A SEM image of a real fabrication disaster is shown>here the e-beam dose was too low. The backbone gate is completely missing due to a too low dose. The written gates were so thin that they lifted up from the wafer surface and are lying loosely around. In Figure 12B an SEM image of a device with a too high e-beam dose is shown. The resist channels collapsed and the evaporated metallic gates turned out to be misshaped.

The thickness of the 4% PMMA spun for 1 min at 4000rpm is approximately 200 nm. If using a more dilute solution of PMMA, a thinner resist layer can be achieved. A 2 % PMMA solution can produce a 50nm layer [39], which can allow a much finer gate pattern. However the mesa and the ohmic contacts are in the order of 200 nm in width, there is a risk of not covering corners of the mesa and ohmic pattern, with a potential short out of the individual gates.

When exposing such a large arrays of gates, due to backscattering from the wafer, the actual dose that each gate gets is higher than if fabricating a single line of the same thickness. This phenomenon is called a proximity effect. The tips of the gates and places, where the gates are more spread do not get as much backscattering, as the middle of a dense gate array. This effect often makes the tips of the gates to get underdosed compared to the rest of the pattern, which leads to the loose and broken tips. This problem can be

solved by dividing the exposed pattern into the main areas and the tips or standing-alone gates. The tips and single gates can then get a slightly larger dose than the array of the gates and create a pretty pattern.

An e-beam lithography system divides all the designed patterns into dots, and exposes each dot for an amount of time given by the dose. There are therefore two ways of defining a thin line: by drawing a long rectangle, or by drawing a line that will be one pixel in width. Obviously, a single pixel line would be thinner. A recipe for fabrication of such lines was developed for both Elionix and E-line lithography systems available in the lab. The produced gate patterns are indeed very fine (see Figure 13), however, the success rate for such a fine pattern is not very high, the gates for the measured devices were therefore written as rectangular areas.

The e-beam resist used for the fine gates pattern has to be distributed evenly on the surface of the wafer, if any particles lie across the gate pattern there would be holes in the gates. The resist that was used for preliminary testing of the recipes for the fine gates was overdue and contaminated. There kept appearing random holes in the produced patterns.

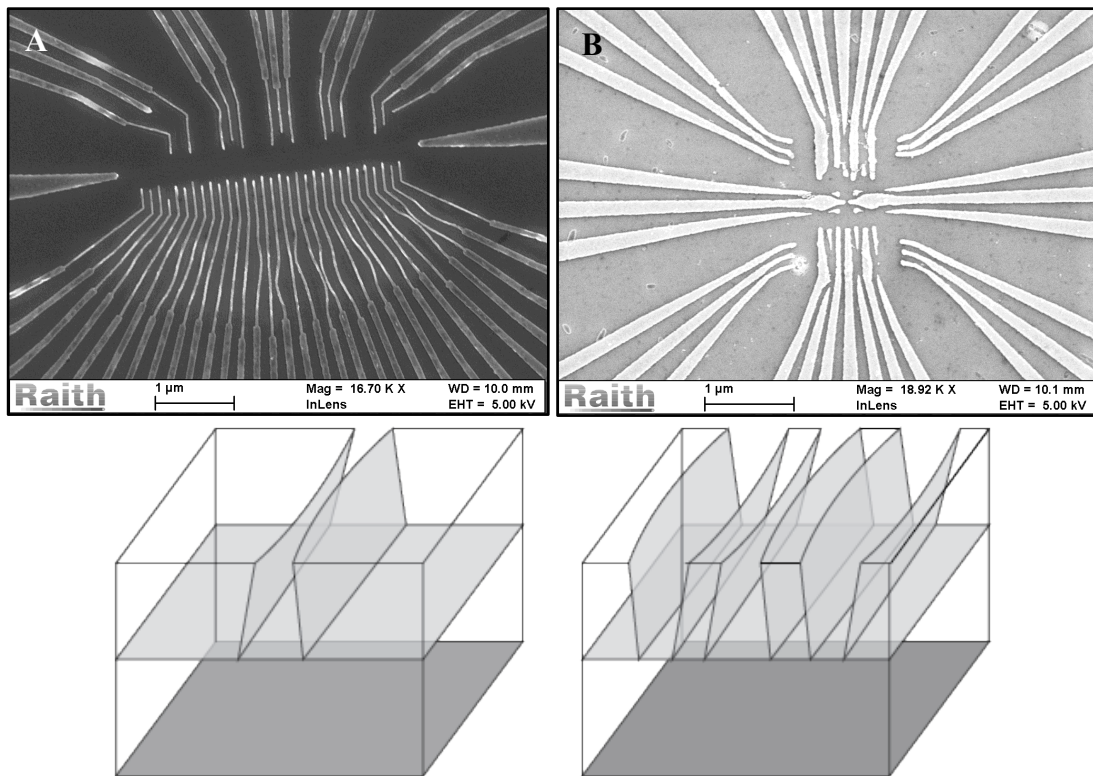


**Figure 12. Wrong dose used for the fabrication.**

A. SEM image of a device with 15 quantum dots in a row written using single pixel lines. In this case the dose for e-beam lithography is too low, the metallic gates are so thin that they come loose. B. SEM image of an overdosed gate pattern. The resist channels collapsed for every second gate in the array. Underneath each image there is a schematic illustration for what happens with the e-beam resist before the metal evaporation, that causes these failures.

As soon as the old bottles of resist were changed to the fresh and clean ones, with one-time use only disposable pipettes, the amount of failed gate patterns reduced drastically. The low success rate of the single pixel line gates could have been due to an old resist. In order to get rid of all the unwanted resist in the written pattern after the development, there was implemented an idea for cleaning wafer with argon plasma right before depositing metal. The success rate for the gate patterns went up, and a number of the devices was produced using this method. However during the measurement process, the devices turned out to be impossible to operate, since the argon plasma damaged the 2DEG within the written pattern. For the devices shown in this thesis, no ashing during the fine gate patterning was used.

#### 2.2.4 Imaging of the devices

The effect of imaging of the devices is yet unknown. A common superstition is that the 2DEG is damaged during the imaging process, as an SEM uses electrons for obtaining the images. To avoid trapped charges the devices are usually not imaged. A study by Nobuyuki Tanaka and Tomonori Ishikawa from 1994 [40] suggests that the electrons reduce the 2DEG mobility if using 10kV e-beam for imaging at a relatively high doses for the 2DEG situated  $\sim 100$  nm underneath the surface. Similar results were obtained in previous studies by Tobin Fink *et.al.* in 1990 [41]. No more articles are published on this topic since 1994, even though imaging is avoided in most experiments. Usually e-beam of 5-10 kV is used for imaging with the Raith system, so the question of the effect of imaging on the 2DEG is relevant. Most of the cooled down samples for this study were imaged and most of those devices showed unexpected behaviour. A further discussion of this topic continues in Section 4.4.

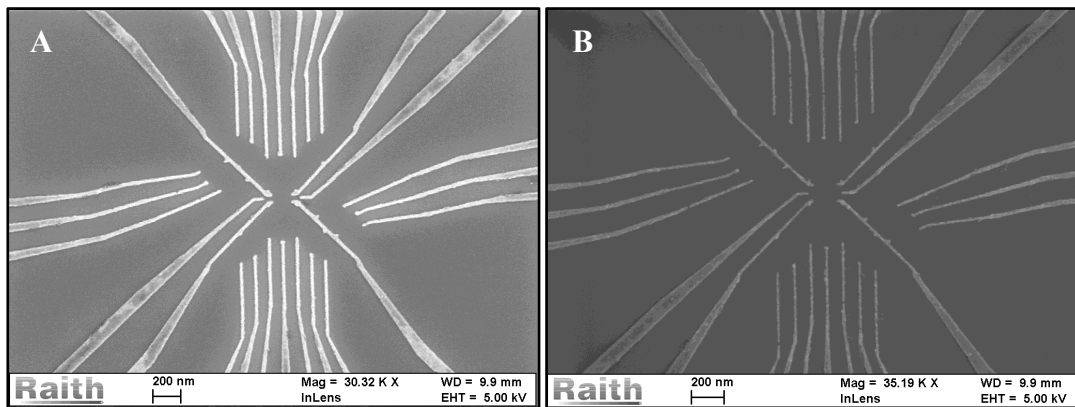


**Figure 13. Single pixel line gates produced with E-line and Elionix.**

A. SEM image of the thinnest single pixel line gates produced using Raith E-line system. B. SEM image of the thinnest single pixel line gates produced using Elionix. The gates produced in Elionix are evidently thinner, however, such fine features might not be necessary, since the success rate on such thin lines is lower than producing the gates using the filled areas.

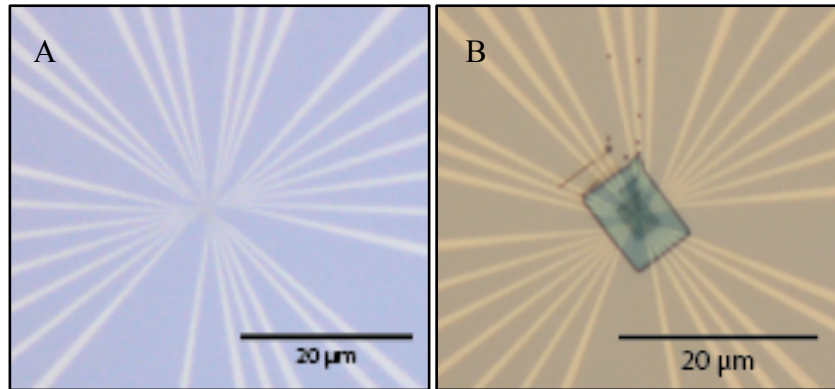


**Figure 14. Cross-linked resist after SEM imaging of the devices.**

A. Healthy chip with no resist on it. B. This device was imaged under SEM, resist left-overs have been remaining on the chip while imaging. Afterwards the device remained having the resist in that area, it was impossible to remove with any solvents or ashing. A device with cross-linked resist was cooled down and showed odd behaviour.

One of the fabricated devices was imaged under SEM after the fine gates step. The remaining e-beam resist from the lift-off was not washed properly off, which lead to a layer of cross-linked resist on the rectangular area that was imaged. The resist remained on the surface: cleaning with hot solvents, ashing or developing did not solve the problem. When measured, those devices with cross-linked resist showed odd behaviour (single channel pinching off the whole ohmic channel, etc.).

## 2.3 The story of the magnets

Production of the micro magnets is an additional step to the device fabrication procedure described in the previous section. This step is executed right after deposition of the fine gate pattern in order to use the alignment marks written in that step. The outer gate pattern does not need a very good precision, as those alignment marks can easily be re-used.

For fabrication of micromagnets, 5nm Ti and 70 nm Co are used; the size of the magnet is chosen to be 100x500 nm. According to a previous study[42], a single cobalt domain has a size of 100x200 nm, which means that produced magnets will contain only two domains and have a tendency to magnetize along the magnet.

### 2.3.1 Alignment

The alignment procedure of fabricating the micro magnets requires very high precision. If the magnet is slightly displaced, it will short out the surrounding metallic gates. An insulating oxide layer can be used between the magnet and the fine gate pattern to prevent the shorting; however if the alignment is poor the magnetic field gradient will not be in the right direction and might not cover the correct dots. Since the high alignment

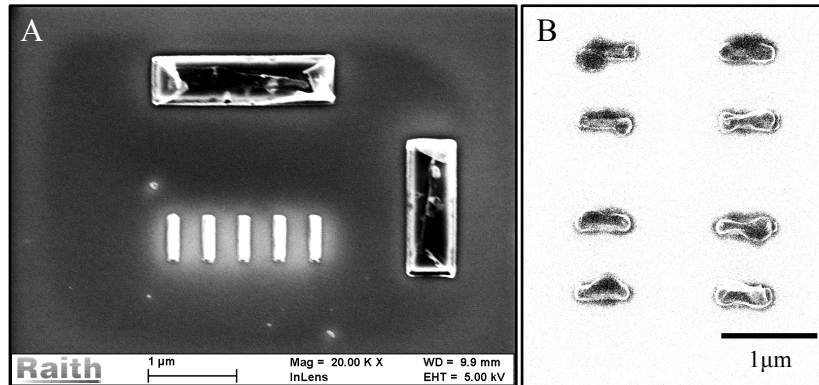


**Figure 15. Misshaped magnets.**

A. An SEM image of a dosetest for micromagnets, the shape seems rectangular. B. An SEM image with inverted colours from another dosetest for micromagnets using a similar dose. These magnets were rectangular in the beginning. The magnets were heated up to 185°C during the fabrication process and changed the shape.

precision is required anyway, the devices are produced without an oxide layer, simply to prevent an additional lithography step.

For the better precision, the alignment marks for magnets are written in the same lithography step as the fine gates. The deposited layer of metal in this step is very thin (5nm Ti, 15nm Au), which makes the alignment marks hard to see in an SEM. The alignment procedure becomes therefore unnecessary hard. All the existing devices were produced using this technique, however for the future devices I would recommend finding another option for alignment (for example adding a quick lithography step after the ohmic pattern and writing an array of alignment marks that will be used for alignment of all patterns). Even though the alignment procedure was hard, alignment precision up to 20 nm was achieved for the produced tests and real devices.

### 2.3.2 Misshaped magnets

The alignment marks for the magnet shape are written in the fine gates step. In order to make sure that those marks are not ruined by the e-beam during alignment procedure, the magnets were written right after the fine gate pattern. In order to make sure that the alignment was all right, the devices were imaged after the last lithography step. Surprisingly, the imaged magnets did have a non-rectangular shape.

For the last lithography step (outer connection layer between the ohmics and the fine gate pattern) the sample is heated up to 185 °C for the resist baking. It turned out that the magnets get misshaped when heated. The same sample was heated one more time for additional layer of gold on the bond pads for a second cool down and the magnets were melted even further. The images of the misshaped magnets can be seen in Figure 15.

A possible solution to this problem could be covering of the magnets with a layer of gold: 5nm Ti, 70 nm Co, N nm Au. A layer of gold could both prevent the magnets from

oxidising and from crumpling up. For the future devices, the magnet fabrication should be the last step in order to avoid the heating of the cobalt film.

## 2.4 Contacting the macro world: Circuit Boards

The area of the fabricated devices is smaller than a square centimetre, and each ohmic pad is 100 microns in width. The size of the measurement apparatus is 10-100 times larger and therefore impossible to apply directly on the devices. In order to get in contact with the macro world, the devices are wire bonded onto printed circuit boards. For this experiment, two different boards were used: the Mayo board and the Sydney board.

For the spin qubit experiments, the sample needs to be cooled down to near absolute zero temperatures. A dilution refrigerator is used for the cool down procedure. The circuit boards have connectors attached that can contact the DC and coax lines inside the refrigerator. The boards are inserted into a cylindrical container, a “slug”, that protects the sample under the loading procedure, helps the cool down and standardises the loading (different boards can be used for the experiments, they are all designed to fit into the same type of slug, that fits the loading system inside the fridge). The detailed description of the fridge is presented in Section 2.5.

### 2.4.1 Mayo board: a “safe” choice

The previous devices with the similar geometry were measured using the Mayo board, designed for the Mayo Clinic in 2012. The board has a 51-pin nano-D connector, as well as 11 SMP coax connectors, which together with the fridge setup allows up to 48 DC lines, 7 coax lines and 4 tank circuits, that are all connected to the 11<sup>th</sup> coax line. Each coax line is connected to one of the 48 DC lines via a bias tee. These boards have shown stable performance and no leakage, the tank circuits were already calibrated for similar devices. The Mayo board is indeed the safest choice for circuit board, due to the previous experiences.

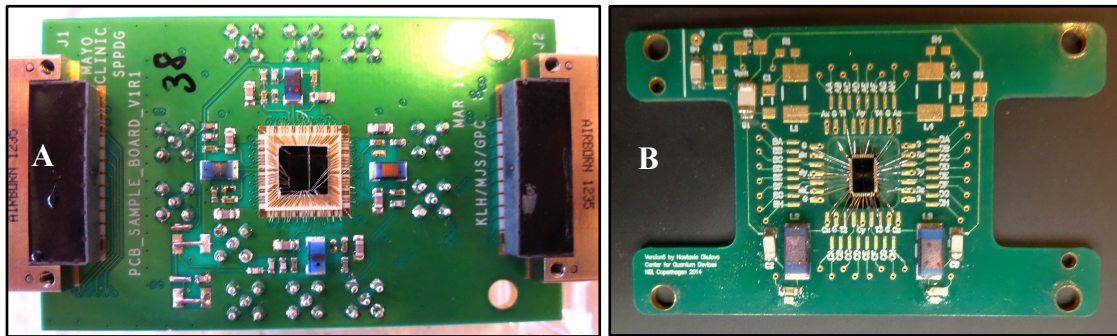


**Figure 16. The Mayo board and Sydney sample board.**

A. Picture of a Mayo board with a device bonded to it. B. A picture of a sample board for the Sydney board with soldered components for two tank circuits and a device bonded up.

#### 2.4.2 Sydney board: new possibilities

The Sydney board was specially designed by James Collins from the University of Sydney for the experiments with many high frequency lines. The board contains 74 DC lines and up to 36 high frequency lines each connected to one of the DC lines via a bias tee. The innovative part for this board is the separate sample board, which is attached to the main board via an interposer. The interposer uses spring-like fuzz buttons that allow the sample board to efficiently contact the pads on the main board. The sample is bonded directly to the sample board. That way, the main board with all the filters and connectors remain in use, while the samples can be easily interchanged without being taken off and re-bonded back again.

The boards are originally designed with two 37-pin connectors. These connectors do not match the connectors in the slug, where 51 pin nano-D connector is used. The boards are fitted into the slugs with the help of an adapter cable assembly that connects the two 37-pin connectors into the two identical 51-pin connectors on the top and the bottom of the slug. A picture of the whole board inside the slug connected via the cable assemblies is shown in Figure 17.

A custom sample board was designed for the spin qubit experiments. The fridge is limited by 48 DC lines and the slug has only 14 coax connectors. The total number of DC lines could therefore not be higher than 48. For the reflectometry measurements, 4 tank circuits are mounted directly on top of the sample board, all 4 tank circuits are connected to the same coax line, but 4 different DC lines. The design of the sample board is presented in Figure 16. For the pin-out, see Appendix C.

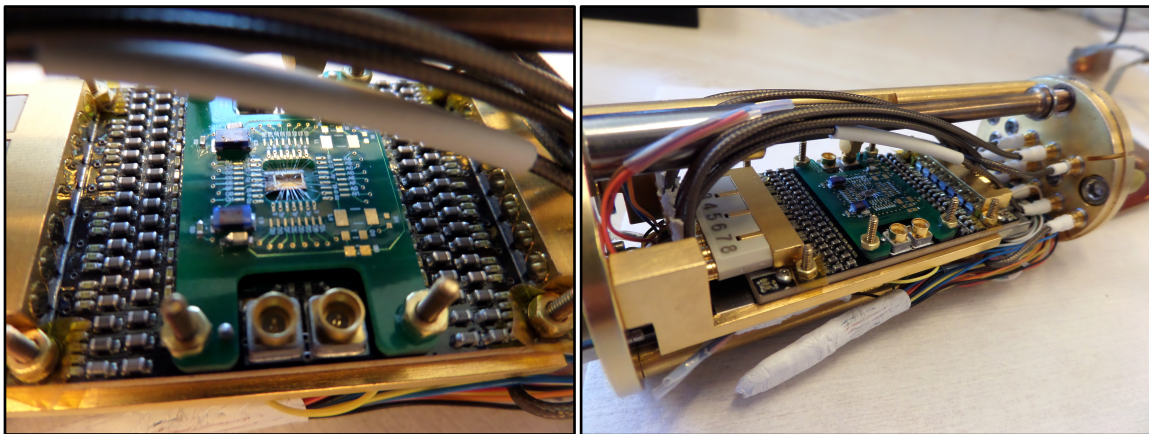


**Figure 17. The Sydney board mounted into the puck.**

The board is mounted into the slug with the help of the mounting brackets. The mounting bracket is isolated from the board via mylah tape to prevent the leakage of the wiring on the board that are in direct contact with the mounting brackets.

### 2.4.3 Wire bonding issue

The samples are connected to the circuit boards using wire bonding. During the bonding procedure, an aluminium wire is pressed into contact with the bond pads on the sample in one end and with the pads on top of the board in the other end. For some reason, many bonds were popping off the bond pads on the sample, either due to the wrong bonding parameters, or due to the annealed contact pads. The layer of gold on top of the pads was falling easily off together with the bond.

The issue was partially solved by re-adjusting the bonding parameters: the “force” and the “power”. Another possible explanation for the problems with bonding could lay in the process of annealing. The heating of the metal stack of the ohmic contacts makes the surface of the ohmics porous. This might prevent the Al bondwires from attaching well to the surface of the pad.

## 2.5 Dilution refrigerator

In order to perform measurements on quantum dots, the device needs to be cooled down to a temperature close to absolute zero for several reasons. For the first, the 2DEG forms at low temperatures. The high mobility and long mean free path in a 2DEG is first achieved below 1K [12]. For the second, the material, and most importantly, the electrons can undergo vibrational excitations, while at high temperatures. To make sure that no unwanted excitations occur during the measurements, the sample is cooled down to temperatures down to tens of mK. For the third, the lower the temperature, the longer decoherence time, due to the inverse proportionality between the spin relaxation time and the temperature of the electron. The last important point is the magnet that generates the constant magnetic field for the Zeeman splitting. The magnet consists of superconducting materials and needs to remain at low temperatures in order to produce a constant magnetic field.

### 2.5.1 The fridge

The procedure of cooling down the sample is executed in an Oxford Instruments Triton™ 200 helium dilution refrigerator. The key operation principal of the fridge is diluting liquid  $^3\text{He}$  into liquid  $^4\text{He}$ , which can bring the system down to few mK. The cooling takes place inside the dilution unit, where the helium circulates. The pre-cooling of the fridge is executed via the pulse tube generator, that provides cooling down to 4K. The cooling power is obtained by compressing and expanding the helium gas within a closed circuit. The system is “cryogen-free”, which means that the cooling procedure is done without using up any helium. For more information about the fridge circuitry and the operation principals, advice Martin Kufahl’s master thesis [37]

The inner part of the fridge is isolated from the room temperature by 4 layers of thermal shields, each layer isolated by vacuum (outer vacuum chamber). The cylindrical shields are attached to the circular plates: the OVC plate, PT1, PT2 and the still. The plates are indicated in Figure 18. The outermost shield encloses all the cooled down electronics and is assembled tightly, so no leaks can get through.

The particular Triton system used for the experiments in this thesis is cryostat nr. 5, located at the Centre for Quantum Devices, the fridge was originally used in Harvard by Jim Medfort and Christian Barthel for the previous spin qubit experiments [12, 13]. 8 coax cables and 48 DC lines run through the middle insert in the plates (plus 2 readout coax lines running through the side insert), and have connectors on the top of the fridge and underneath the MC plate, where the connectors are attached to the slug. The sample has contact with the mixing chamber plate via the PCB, the puck, the mount and all the connectors, the direct physical contact of the metal surfaces ensures the cool down.

The DC lines run through a number of filters and the coax lines have attenuators attached after every plate. The schematics of the lines inside the fridge is illustrated in Figure 18A. Each DC line goes through an RC and RF filter. The overall resistance of each line is therefore determined by the resistors on the sample board and the RC filters.

#### 2.5.2 Puck and loading procedure

The Triton 5 fridge allows a loading procedure without warming up and cooling down every time the sample change is needed. The sample is placed inside a so-called slug (also known as puck), where the sample board is attached to all the connectors that will during the loading be attached to the connectors inside the fridge. The upper part of the slug has 14 SMP connectors and a 51-pin nano-D connector that match the connectors on the “cold finger” inside the fridge. The cold finger is thermally connected to the mixing chamber, so the puck is cooled down via the contact between the slug and the cold finger.

The loading procedure is executed using a puck loading stick that can be attached to the bottom of the OVC. The puck loading stick has two rods, which are used for guiding the sample inside the fridge up to the cold finger. The puck is being screwed into the cold finger and out of the guiding rods; the puck loading stick can be detached from the fridge afterwards.

An important safety precaution during the loading procedure is collecting all the  $^3\text{He}/^4\text{He}$  mixture and storing it in a tank outside the fridge. This makes sure that the room temperature puck that is being inserted into the fridge does not heat up the mixture and create an overpressure.

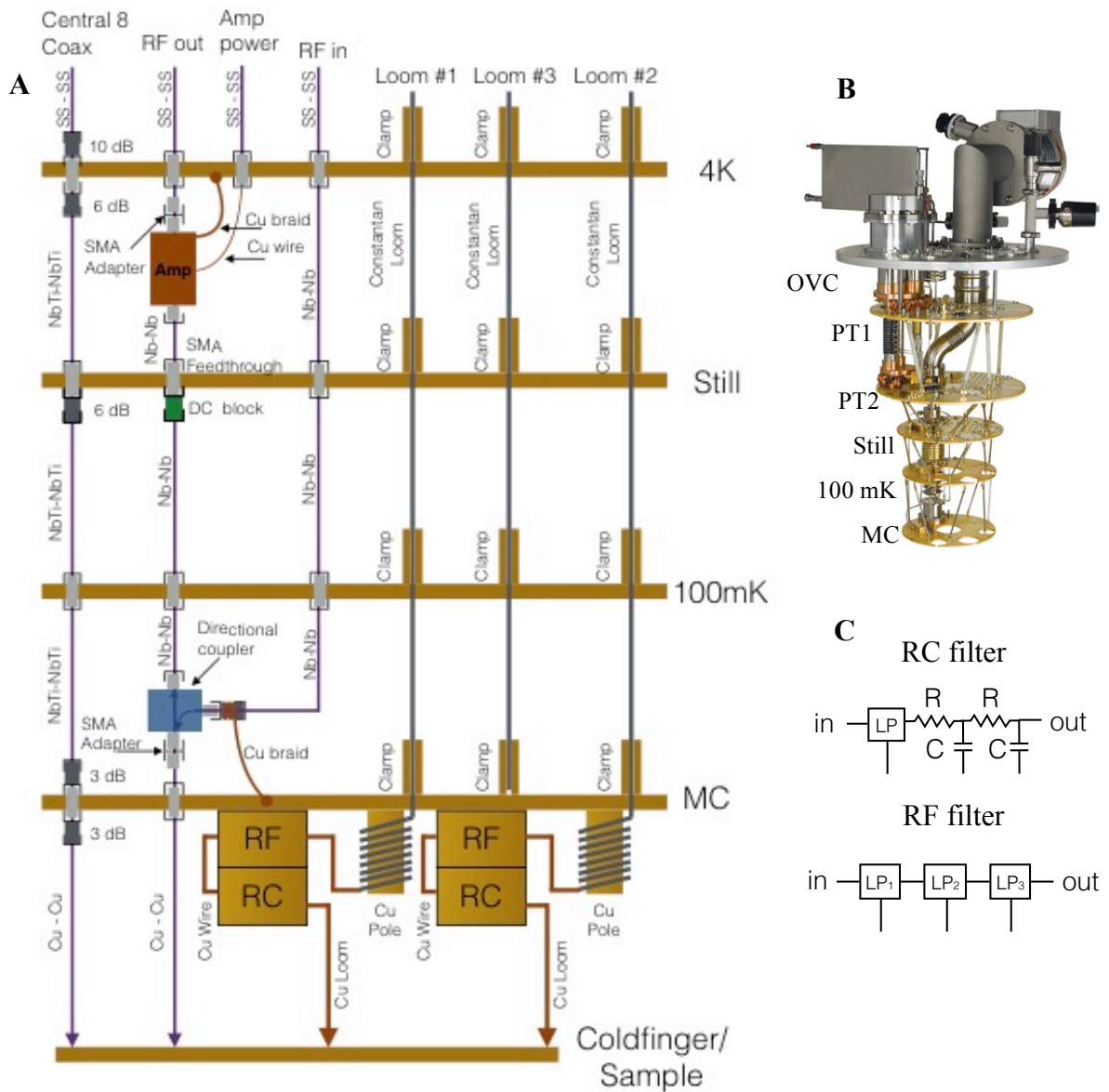


**Figure 18. The layout of the Oxford Instruments Triton™ 200.**

A. The schematics of all the lines running through the fridge adopted from Johannes Bail's thesis. The 11 coax lines are shown on the left, including all the attenuators. The RF in and out lines are used for the fast readout. The three Looms on the right include 24 DC lines each, but only two of those are connected to the nano-D connector on the cold finger. Loom 1 and Loom 2 go through RC and RF filters, the schematics of the filters are shown in figure C. B. The schematics of the plates inside the fridge. The wires shown in figure A are connected through the middle insert or through the peripheral opening in the plates. OVS, PT1, PT2 and Still plates hold the thermal isolation shields. C. The schematics of the RC and RF filters for the DC lines. The values for the RC filter: LP = 80 MHz, R = 2 kΩ, C = 5 nF. The values for the RF filter: LP1 = 80 MHz, LP2 = 1450 MHz, LP3 = 5000 MHz

## 2.6 Measurement setup

All the DC and coax lines shown in Figure 18 have a contact to the sample via the coldfinger and the puck. Those lines go through the cooling parts of the fridge, attenuators or filters and come out on top of the cryostat. In this section a layout for the cables outside the fridge and measurement setup connected to the fridge are described.

### 2.6.1 DC transport equipment

Only two of the three looms shown in Figure 18 are connected to the nano-D connector in the puck. Those 2x24 DC lines are connected to 2x24 pin Fischer connectors on the top of the fridge. Each Fischer connector is plugged into a breakout box that is fixed on the rack outside of the fridge<sup>2</sup>. The breakout boxes have a BNC connector for each of the 48 DC lines. Each line has a switch that offers choices between “ground”, “bias” and “on”. The “ground” position connects the line with the fridge ground. The “on” position connects the line directly with the electronics that is connected to the breakout box via a BNC cable. The “bias” line connects the fridge line to the breakout box bias line, that is shared between all the lines on the breakout box. If connecting the bias line to a voltage source, the same voltage would apply for all the lines that are switched to the bias line.

All the depletion gates and ohmic contacts on the device need a controlled voltage source. All those lines are connected to the digital-to-analogue converters (DACs) that can supply the gates and channels with a chosen voltage. Each DAC line is connected to the correct gate on the breakout box via a BNC cable. For a better resolution, a 5:1 voltage divider is connected to each DAC channel. For the channels connected to ohmic contacts, the 1000:1 dividers are used. The ohmic channels are operating in the range between -1mV and 1mV and the depletion gates operate between 100mV and 1V, which makes the resolution precision less important for the depletion gates. Each DAC channel is additionally connected to a low-pass filter, for the high frequency noise filtering. Each DAC channel is connected directly to the acquisition computer that can control the DAC voltages.

The DC lines are used for setting voltage through the gates and measuring the device in a transport and charging regime. For recording the data from transport measurements through the dots and sensors, the digital multimeters (DMMs) are used. DMMs use a voltage signal for the input, which means that the current running through the device needs to be converted into voltage. A current preamplifier, called Ithaco<sup>3</sup>, is used for that purpose.

---

<sup>2</sup> Breakout boxes on Triton 5 are situated in a reachable height for an average person (unlike the old breakout boxes on Triton 7).

<sup>3</sup> Ithaco Precision Instrumentation Division model 1211 produced by DL Instruments



### 2.6.2 The fast gates and electronics

In Triton 5 there are 8 coax lines connected to the coldfinger, plus a readout line for the reflectometry circuits. The coax lines go through the cooling part of the refrigerator, connected to a number of attenuators and end up with SMA connectors on the top of the fridge. The fast lines are used for reflectometry measurements and pulsing (see chapter 3 for more details on the measurements).

For the fast readout the oscillating signal on the fast gates is generated by the right and the left ramps. For the custom pulse sequences for pulsing across the transition on the charge stability diagram, the pulses are generated via an arbitrary waveform generator (AWG). Both ramps are synchronised with the AWG, which lets use of the same gates on the device to be used both for the fast readout and pulsing simultaneously. The experimental setup with all the used electronics is described in Figure 19. The measurement techniques are described in the next chapter.

## Chapter 3. Measurement techniques

---

After the devices are fabricated, bonded and secured inside a puck, the cool down and measurement phase can begin. The basic measurement setup needs to be prepared before inserting the puck into the fridge. First, the setup and lines are tested. Then the sample is connected with the data acquisition system (those steps are described in Section 3.1).

From the past experiences, the devices are proven to become more stable if applying a positive bias on the gates during the cool down. The positive voltage is set on each gate and kept constant until the chip has reached the base temperature. After the bias cooling, all the gates and ohmic contacts are tested and a decision is taken, whether the device has potential for further measurements.

The working devices proceed to the transport measurement stage, where the transport through the ohmic channels is measured. The depletion gates are used to confine quantum dots in the 2DEG. For better signal, the same dot region can be measured using the transport through a sensor quantum dot. The sensor dot can as well be used for the reflectometry measurements. All the measurement stages are described in Section 3.2-3.4

### 3.1 Bias cooling and testing the device performance

The bias cooling procedure has been used for similar chips on the same type of wafers for many generations of devices. The idea behind this technique is reducing the charge tunnelling through the Schottky barrier and with that reducing the switching behaviour (if charges tunnel in or out of the quantum system, the electrostatic environment changes drastically; when this happens more frequently then the measurement time, the measured graphs are hard or impossible to analyse). The method is proven effective, though it is hard to point out a correct value for bias cooling. Usually the applied bias is chosen empirically by re-cooling the devices and seeing if the signal to noise ratio has improved. The wafers used for fabrication of devices presented in this thesis have shown low switching rate for the values of bias cooling between 50 and 350 mV.

For the bias cooling procedure the bonded device is fixed inside the puck, where it is connected to all the planned DC and coax lines. While bonding, all the DC lines on the board are shorted together and connected to the ground of the bonder to prevent blowing up the device. After bonding, the DC lines are kept shorted out, when inserted into the puck, the connector on the outside of the puck is shorted together as well and connected to the ground. When attaching the puck to the load lock, the load lock needs to be connected to the ground of the fridge, such that the attached puck would also be connected to the fridge ground.

### 3.1.1 Bias cooling

Before attaching the puck onto the loading stick, all the equipment has to be tested: The DECA DAC channels have to be calibrated, the connection to the Keithley and DMM's needs to be verified and the equipment tested (for example by sending current through a known resistor and measuring the voltage drop). Then two breakout boxes need to be attached to the puck loading stick (number of breakout boxes depends on the looms the bias cooled lines are going to be connected to, if the lines are distributed along the two looms, there should be two breakout boxes). All the lines on both the Triton breakout boxes and puck loading stick bob's should be grounded. The Keithley is connected to all the bias lines on each bob. Now the puck can be connected to the puck loading stick and attached to the fridge. The air is pumped out of the load lock and the ohmic contacts are tested. If all contacts are working, the bias cooling procedure can begin.

First all the bias cooled lines are switched over to the "bias" line on the breakout boxes, both on the load lock and on the fridge. Then the voltage on the Keithly is ramped up to the desired value. The loading procedure can begin. The fridge gauge valve is opened,

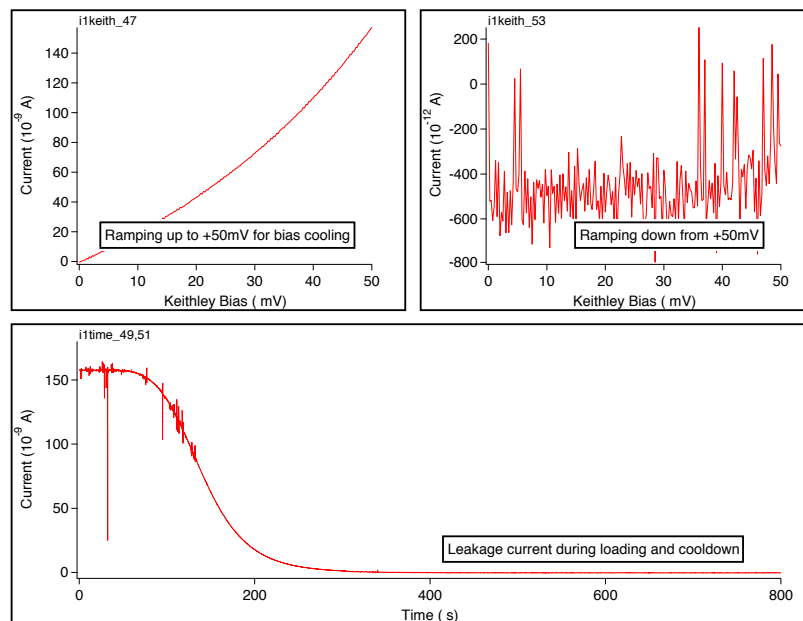


**Figure 20. Monitoring the bias cooling.**

First the voltage on all the bias cooled lines is ramped up to the wished value. If the leakage current appears to be much larger then hundreds of nA, there are most probably shorted gates somewhere and the device is not useable. Then the device is loaded. The spikes on the lower graph indicate any mechanical distortions of the system: hitting the coldfinger with the puck, screwing the puck into the coldfinger, sliding the puck loading stick out of the OVC. After the device is cooled down, the bias voltage is ramped back down to zero, the leakage current should remain constant and be close to zero.

puck inserted and screwed tight onto the cold finger. The puck loading stick is then taken out of the fridge and can in principal be taken off<sup>4</sup>. The leakage current is monitored during the cooldown. GaAs is conductive at room temperature, which explains the high current value in the beginning. As the device is cooled down, the value of the leakage current should approach zero (or a value close to zero).

When the device is cold, the bias voltage can be ramped down to zero and the puck loading stick and the breakout boxes can be taken away. The ohmic contacts are tested again, the resistance now depends on the number of channels open and the in-line resistance of the fridge. When subtracting all the factors, the resistance of the ohmic channels can be calculated.

### 3.2 Transport through a quantum dot

#### 3.2.1 DC measurements

DC transport measurements are executed by attaching a DAC channel to one of the ohmic contacts and attaching a DMM via an Ithaco to another ohmic contact on the device. By applying a small bias voltage (0.05-0.5 mV) on the DAC channel (source ohmic), the current running through the channel can be measured with the DMM (drain ohmic). The channel can be pinched off using the depletion gates (each depletion gate is connected to a DAC channel). The current through the ohmic channel is recorded as a

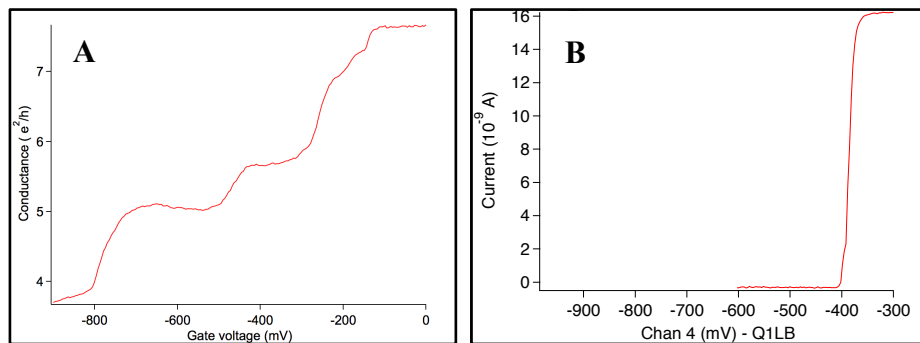


**Figure 21. Pinch-off test.**

A. A good pinch off behaviour, the current does not drop sharply at the pinch off value, but shows a QPC-like behaviour. Measured on device NO9a. B. A pinch-off curve of a gate that cannot form a quantum dot. One interpretation can be that as soon as the gate depletes the 2DEG underneath itself, it pinches off the whole channel.

<sup>4</sup> Every single mechanical distortion in the system creates "spikes" in the measured current. The puck loading stick and bottom breakout boxes were kept on place until the end of the bias cooling process to make sure that no unwanted charges are sent through the system (that can potentially blow up the fine gates on the device). This is probably unnecessary precaution, however we chose better to be safe, then sorry.

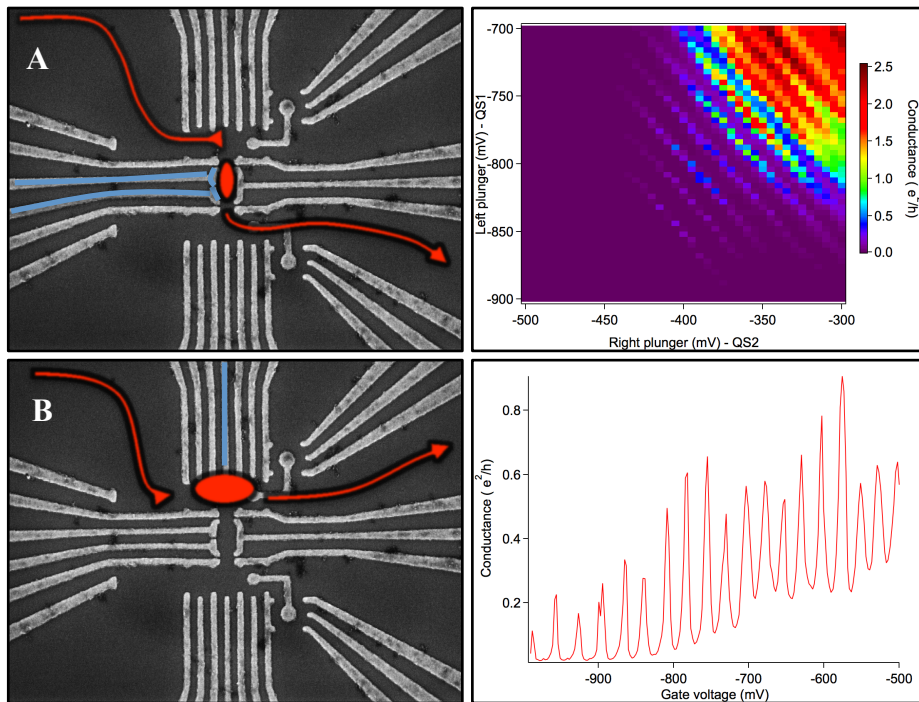


**Figure 22. Transport through a large quantum dot on device NO9a:**

A. Transport through the large quantum dot formed in “sausage” region. Measured on device NO9a. A nice quantum dot is formed. B. Coulomb oscillations in a quantum dot formed in the qubit 2 region, controlled using the middle plunger gate.

function of the gate voltage, an example of a pinch off curve is shown in Figure 21. In Figure 21A, a “healthy” pinch off curve is shown, where the current falls off with a QPC-like behaviour. If the current drops without showing any oscillatory behaviour (the plateaus), the gate most likely pinches the whole channel off as soon as it depletes the 2DEG underneath it.

For most of the cooled down devices gates did not pinch the channels off even though they looked fine under SEM and were bonded with multiple bonds. It is unknown, why bonding some times did not work. By taking the devices out of the fridge and re-bonding the same devices again, the bonds could be fixed.

### 3.3 Charge sensing

The charge sensing technique allows sensing of the electrostatic environment in the quantum dots using transport through an adjacent quantum dot. The idea behind the operation of a sensor is described in Section 1.2.3: a charge sensor is brought into a regime of Coulomb oscillations and left at the middle of a Coulomb peak slope. The changes in the electrostatics around the dot are showing in large changes in the transport signal through the sensor quantum dot (SQD).

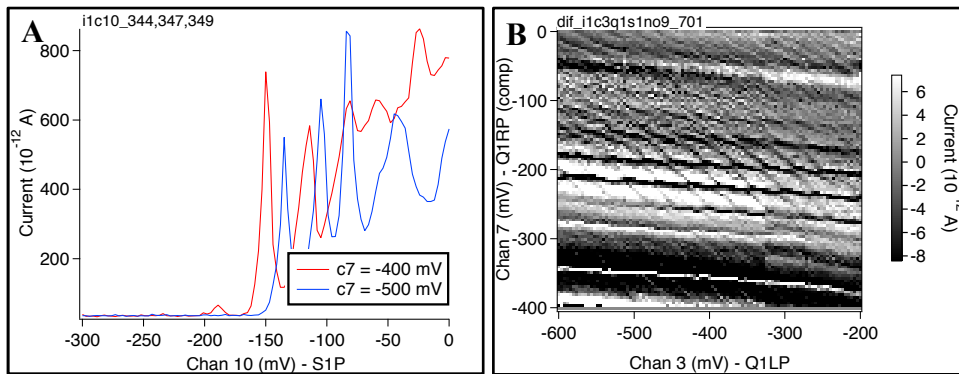


**Figure 23. Setting up the compensation for SQD.**

A. Measuring the shift in the Coulomb oscillations when stepping the nearest plunger in the measured dot. B. Using a linear relation found from fig. A to compensate the plunger of the sensor. The SQD is therefore sensitive on a large area, where double dot Coulomb oscillations can be seen. The presented graph is a derivative of the original current through the sensor.

This technique uses transport through a sensor quantum dot instead of transport directly through the operating quantum dots. The SQD is capacitively coupled to the gates that operate the sensed qubit. Ramping a gate close to the sensor adds extra background to the measurements. The height of the chosen Coulomb oscillation peak in the sensor determines the sensitive area: the sensor slowly “drives” off the peak as the gates close to the sensor are ramped. This issue is solved via compensation of the plunger gate value of the sensor linearly to the value of the ramped gate. For example on when the right plunger in qubit 2 is changed by 100 mV, the Coulomb peaks in the sensor dot move by 20 mV, the compensation factor would be 0,2. The plunger gate of the sensor will then be stepped 20% of the value stepped on the Q1 right plunger. In Figure 23A, the Coulomb peaks in a sensor quantum dot are shown. In Figure 23B, a sensing signal using that sensor dot with the compensation for adjacent quantum dot plunger.

### 3.4 Reflectometry and pulsing

Event though the charge sensors are very efficient and improve the signal drastically, the measurements for a 100x100 graph can take up to 30 min. Even more efficient measurement technique is using the sensor quantum dot in a reflectometry circuit. The described setup was designed By James Medfort and assembled for Triton 5 by Johannes Beil and Tomohiro Otsuka.



The low-pass frequency ( $f_{lp}=1/(2\pi LC)$ ) for the DC measurements using a charge sensor is approximately 1kHz, given that the value for channel resistance is in the order of 100k $\Omega$  and capacitance the loom wires that run through the fridge is around 1nF. This is not fast enough for performing measurements on charge dynamics, which is in a MHz range. A faster measurement technique is needed. In 2007 David Reilly *et.al.* [43] demonstrated using a quantum point contact operating with radio frequency at a nearly pinched-off state for a better and fast sensitivity. In 2010 Christian Barthel *et.al.* demonstrated a similar concept for the use of radio frequency reflection off a sensor quantum dot [19].

The basics of the reflectometry rely on matching impedance of the tank circuit on the measured device with the characteristic impedance of the reflectometry line. The impedance of a tank circuit is given by:

$$Z \sim \frac{L}{RC}$$

where L is given by the inductors, that are located on the circuit board and C is the stray capacitance collected from all the bondwires, 2DEG, bondpads, the fridge etc. and R is the resistance: the measured parameter that comes from the sensor dot signal. If the two values for impedance match perfectly, no signal is reflected, all the power is transmitted to the device. If the impedance values are far away from each other, most of the signal will be reflected.

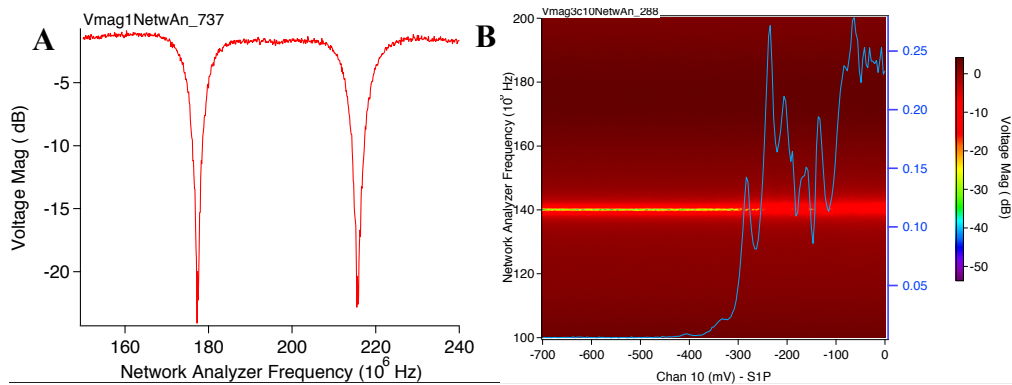


**Figure 25. Measured reflected signal.**

A. The reflected signal measured at room temperature using the Network Analyser attached to the SMP connector that is attached to the tank circuits in the puck. B. The resonance frequency measured in the tank circuit attached to Sensor 1, as the sensor quantum dot is pinched off via the plunger gate (sample NO9b). All the reflectometry data presented in the result section is measured via this reflectometry circuit. The values for the

To measure the reflected signal a demodulation circuit is used. The beam splitter divides the AC signal into two signals with the same frequency  $f$ . One half of the signal is sent into the fridge, where depending on impedance mismatch with the tank circuit at the sample, the reflected signal will come back. The other half of AC signal is sent directly to the mixer. The two AC signals are then mixed together.

Since the frequency of those two signals was the same to begin with, the mixed signal will have a double frequency component  $2f$ , and a DC offset. The  $2f$  frequency can easily be filtered out and the resulting DC signal is measured by the Alazar card (the signal is measured in voltage, so it can in principal be measured by any voltmeter).

It is important to choose the RF frequency and the circuit components such that the  $50 \Omega$  matching happens around the sensitive area of the charge sensor which is implemented as a resistive element in the tank circuit. In Figure 25B the RF signal goes through matching as the sensor quantum dot pinches off.

The speed of a measurement with the reflectometry signal is two orders of magnitude higher than the speed of the charge sensing recording. The same fast gates are connected to the AWG, which is synchronised with the ramp. The AWG can be used for pulsing in any direction and in any sequence on the charge stability diagram.

## Chapter 4. Results and experiences

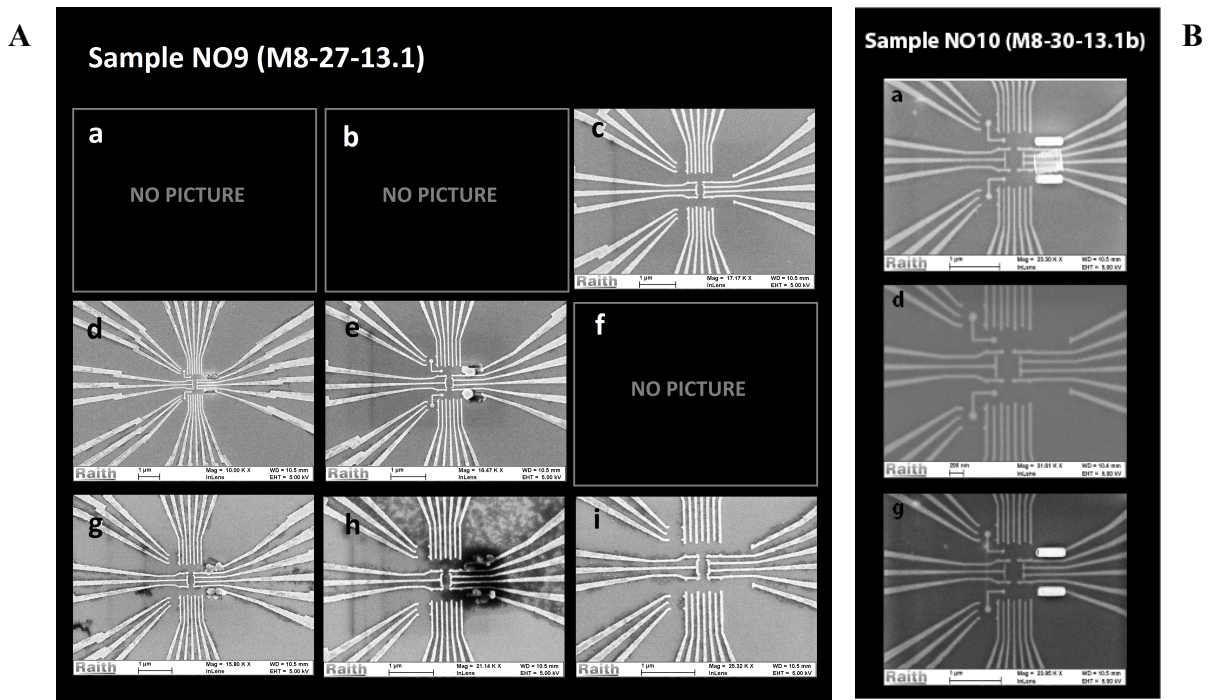


**Figure 26. The fabricated devices.**

A. NO9 a-i. Wafer: M8-27-13.1: electron mobility  $\mu = 2,3 \times 10^6 \text{ cm}^2/\text{Vs}$ ;  $n = 2,5 \times 10^{11} \text{ cm}^{-2}$  uniform doping. The chip is cut out of the edge of the wafer; some of the devices might have low mobility.

B. NO10 a,d,g. Wafer: M8-30-13.1b: electron mobility  $\mu = 3,9 \times 10^6 \text{ cm}^2/\text{Vs}$ ;  $n = 1,2 \times 10^{11}/\text{cm}^{-2}$  uniform doping. The chip is cut out of the edge of the wafer; some of the devices might have low mobility.

Many different iterations of the chosen geometry were fabricated for this experiment. An overview of the devices is shown in Figure 26. The devices were fabricated with and without the magnets and with and without the couplers. The devices were fabricated on two different heterostructures: M8-27-13.1, where the 2DEG is situated 57 nm below the surface and M8-30-13.1b, where the 2DEG is situated 91 nm below the surface of the wafer.

Unfortunately, due to the melted magnets, none of the fabricated magnetic samples were used in this study. For future experiments, the magnets should be fabricated as the last step and the sample should not be heated after the fabrication is completed. The samples with melted magnets were cooled down, however, all the cooled down samples had a failure mode.

Most of the fabricated devices were cooled down, though only few showed a potential for forming quantum dots. The complete overview of the cooled down devices and failure modes is presented in Appendix B. The data presented below is measured on device NO9b; the device has no magnets, but does have the “couplers”. There is no micrograph

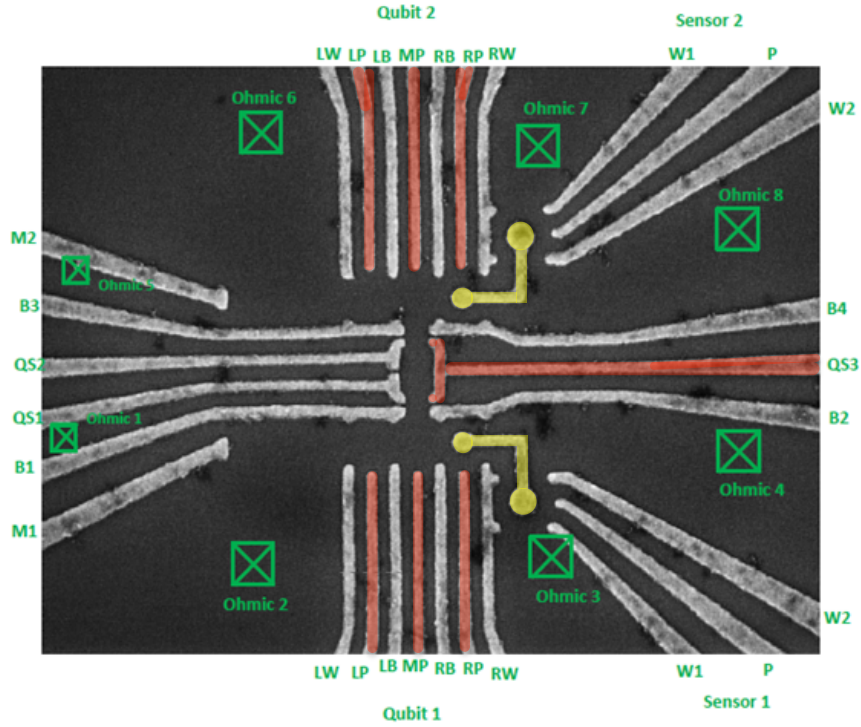


**Figure 27. An SEM picture of a device identical to the one measured in this study.**

The schematics for the gates: The three dots in the lower position are noted as Qubit 1, the potential dots are noted left, middle and right dot. The sensor associated with the three dots is called Sensor 1. A similar nomenclature is used for the dots in the upper region. The “big” connector dot in the middle is formed using gates QS1, QS2 and QS3<sup>5</sup>. The gates connected to the coax lines are marked with red, the coupler floating gates are yellow.

of this actual device, a device identical to the measured one is presented in Figure 27. The device was bonded onto a Mayo board with two tank circuits.

## 4.1 Repeating past experiments

In order to test the performance of a device with a coupler situated between the sensor quantum dot and the qubit quantum dots, basic operations on a conventional double quantum dot are performed. The nomenclature for the gates on the measured device is presented in Figure 27, the same nomenclature is used throughout the whole chapter.

### 4.1.1 Double dot

A double dot, shown in Figure 28B, is formed in Qubit 1 position in the middle and right dot, using the transport from Ohmic 2 to Ohmic 4 (0,1 mV bias). Both dots have

<sup>5</sup> The QS stands for “Quantum Sausage”, the dot has the name “sausage” because of the prolonged shape. In principal, this dot does not have to be formed as a sausage, as long as it has discrete level spacing and large electron occupancy.

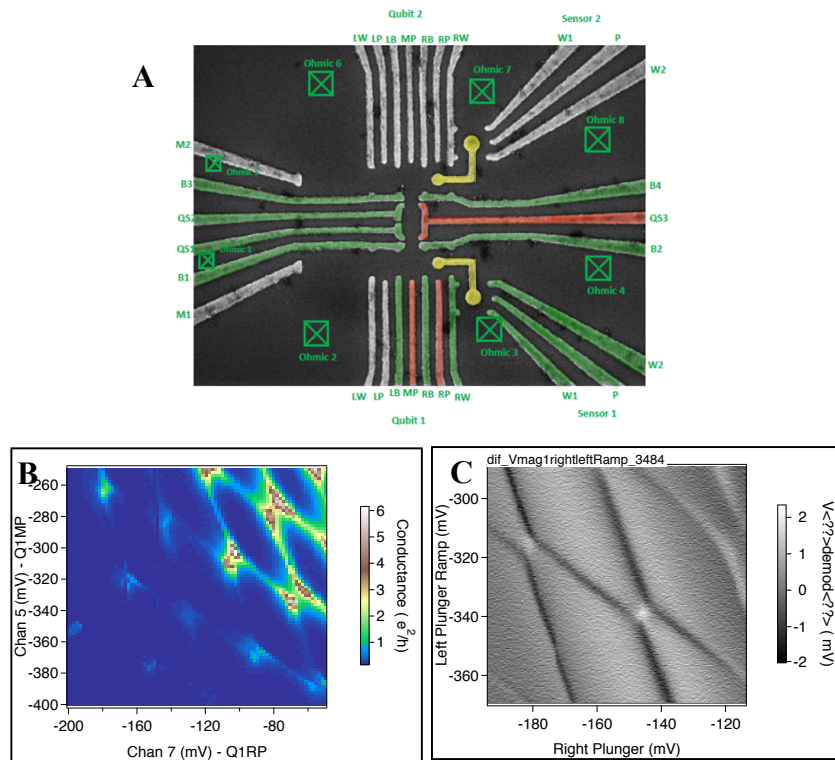


**Figure 28. A double dot formed in the Q1m and Q1r positions.**

A. SEM image of the device with the energised gates marked with green and red. B. Coulomb oscillations measured using transport through Ohmic 2 – Ohmic 4 channel, bias of 0,1 mV. Transport through a double dot can be seen. C. Transport through the sensor dot, Ohmic 3 – Ohmic 4, 0,1 mV bias. C. Sensing the double dots using the sensor dot.

unknown occupancy. If trying to empty the dots for the electrons, the Coulomb oscillations continue, though we were unable to find the last electron due to latching. The transition seen in the figure is at least 10<sup>th</sup> electron for both dots (it was possible to empty 10 electrons out of each dot and there seemed to be more Coulomb oscillations). Since the occupation is random, the chance of having an equal number of electrons in each dot is very small, hence, the double dot is asymmetrical.

The transport through the sensor dot is tuned up and the most sensitive oscillation of the dot is chosen for the charge sensing measurements (Figure 28B). The charge stability diagram is measured using the sensor dot and the result is visible in Figure 28C.

#### 4.1.2 Spin blockade

A double quantum dot with an odd number of electrons in one of the dots and even number of electrons in the other dot can be brought into a spin-blocked regime. Pauli blockade should thus be visible in every second transition between the dots. In order to see the spin blocked regime the coupling between the two dots needs to be just right. When the tunnelling barrier between the dots is too high, the coupling between the two dots is too weak, so the tunnelling rate goes down. When the tunnelling barrier is too low,

the coupling is too strong; as a result, the electrons travel freely between the two dots: they practically melted into one large quantum dot. The examples of too open and too closed tunnelling barriers are presented in Figure 29A,B,C. When the occupancy of the dots is unknown, the odd/even number of electrons can be calculated from observations of spin blockade.

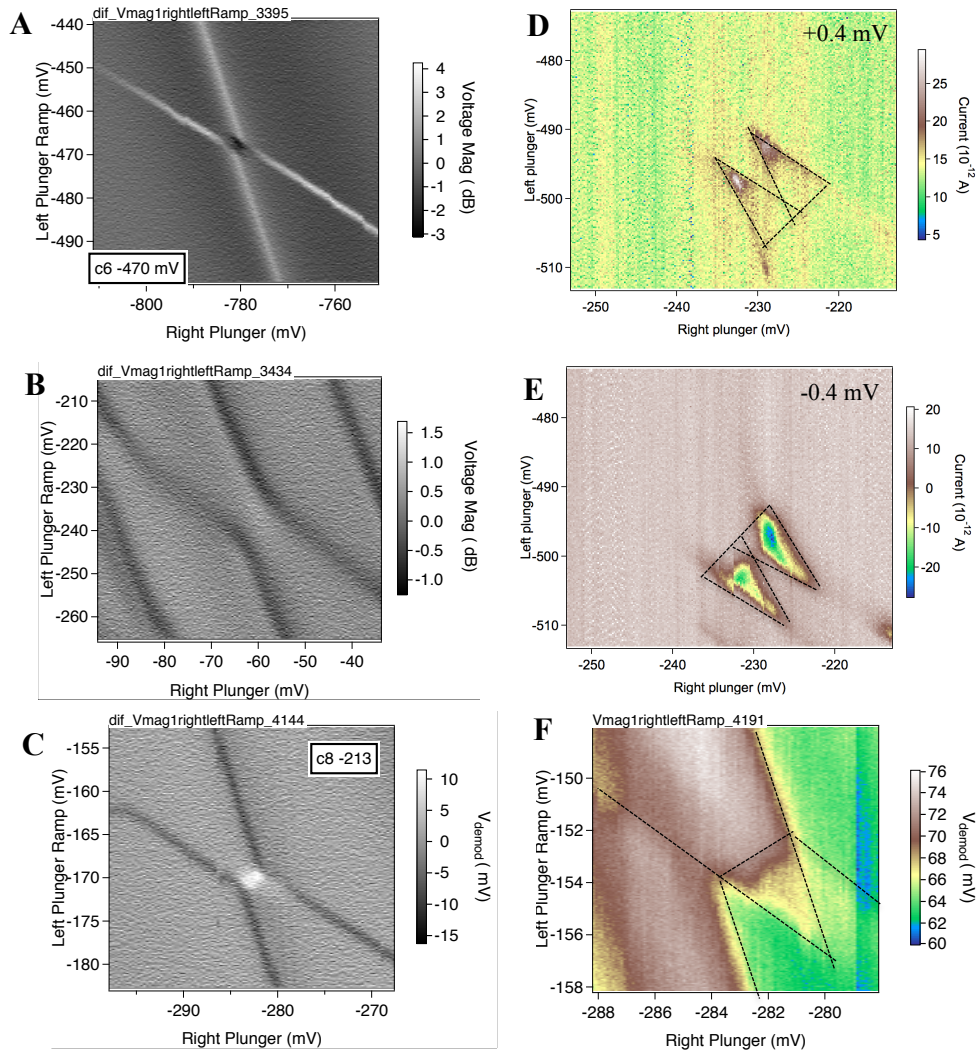


**Figure 29. The coupling between the dots and a spin blockade.**

A,B,C. Charge stability diagrams, Qubit 1 Right plunger voltage is plotted against the Middle plunger voltage. On graph A, the barrier between the dots is too pinched off, on graph B the barrier is too open. On graph C the barrier is tuned right, if there is possibility for spin blockade, it should be possible to see it in a transition tuned into this regime. D,E. Transport measurements through the double dot. The bias triangles might indicate a sign of the spin blockade. The applied bias is 0.4 mV/-0.4mV, as indicated in the figures. F. A spin blockade is observed in a double dot applying linear pulses directly over the transition.

Spin blockade was measured using transport measurements through the double dot. When applying positive and negative bias, the bias triangles in the blocked transition would be truncated and the size of the triangles created by positive and negative bias would be different. The bias triangles measured in the double dot are shown in Figure 29D,E. The particular transition did show sign of spin blockade, the triangles in Figure 29E are obviously larger than the triangles in Figure 29D.

The spin blockade was observed in a neighbour transition, when applying linear pulse across the transition line. The indication of the spin blockade disappeared when pulsing time was increased to 4  $\mu$ s, which indicates a quite short coherence time.

The fact that a spin blockade could be tuned in these quantum dots tells us that quantum dots with occupancy larger than 10 electrons per dot do not have any degenerate levels. It could also indicate that 10+ electron quantum dots are in total spin  $\frac{1}{2}$  and spin 0 regimes, otherwise the spin blockade would not be observed. This could mean that  $\Delta > u$  (level spacing is larger than the Coulomb repulsion, see Section 1.4.2) for this large occupancy, which shows potential for operations of qubits in regimes of tens of electrons without moving out of total spin  $\frac{1}{2}$  state for the operating quantum dots.

#### 4.1.3 Singlet-triplet splitting and further measurements

Singlet-triplet splitting as a function of time spent in the measurement position was measured using a function written by Tomohiro Otsuka. A switching event brought the system into a different place on the charge stability diagram and the spin-blocked regime was lost. The same quality of singlet-triplet splitting was not possible to achieve. The data from this measurement is presented in Figure 30.

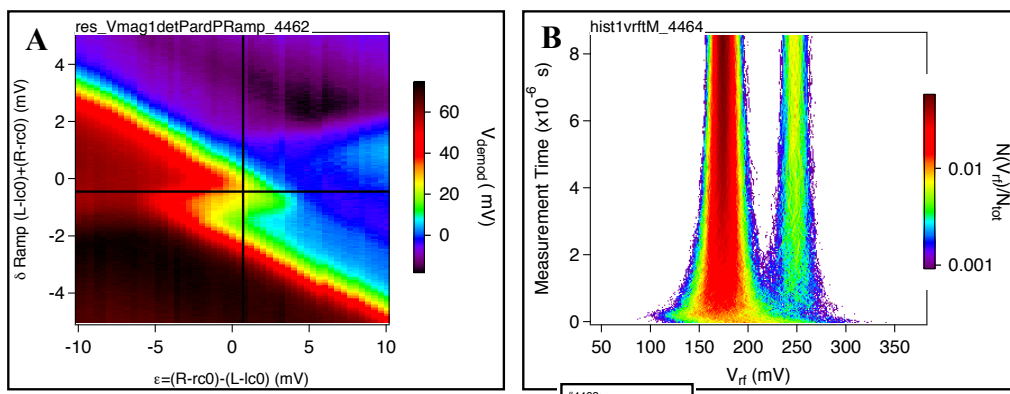


**Figure 30. Singlet-triplet splitting.**

A. The spin blocked regime plotted in the detuning coordinates. B. Singlet-triplet splitting plotted against the time spent on the measurement position for Pauli-blocked region shown in **Figure 29**, measured using single shot readout.

For proper measurement of singlet-triplet splitting, initialisation and coherent rotations, control software for the fast gate operations is needed. The acquisition code written by Alex Johnson for Harvard laboratory was modified by Christian Barthel and Jim Medfort for the experiments using fast gates. The details about running the code and performing pulse gate measurements stayed in Harvard, and unfortunately there was no time to understand or re-write the pulsing gate control software. Repetition of the same custom pulsing sequence was required for further measurements and therefore unfortunately these measurements were not completed. The next step after separating singlet from triplet would have been performing coherent rotations around the Bloch sphere just as performed by Jason Petta in 2005 [8], using pulse sequences similar to the presented in the article, using the exchange energy for spin manipulations.

## 4.2 Adding a third dot

The second axis of control for the experiment on two electron dots can be achieved by adding an extra electron into the system. For such an experiment, a third dot should be tuned up next to the double dot.

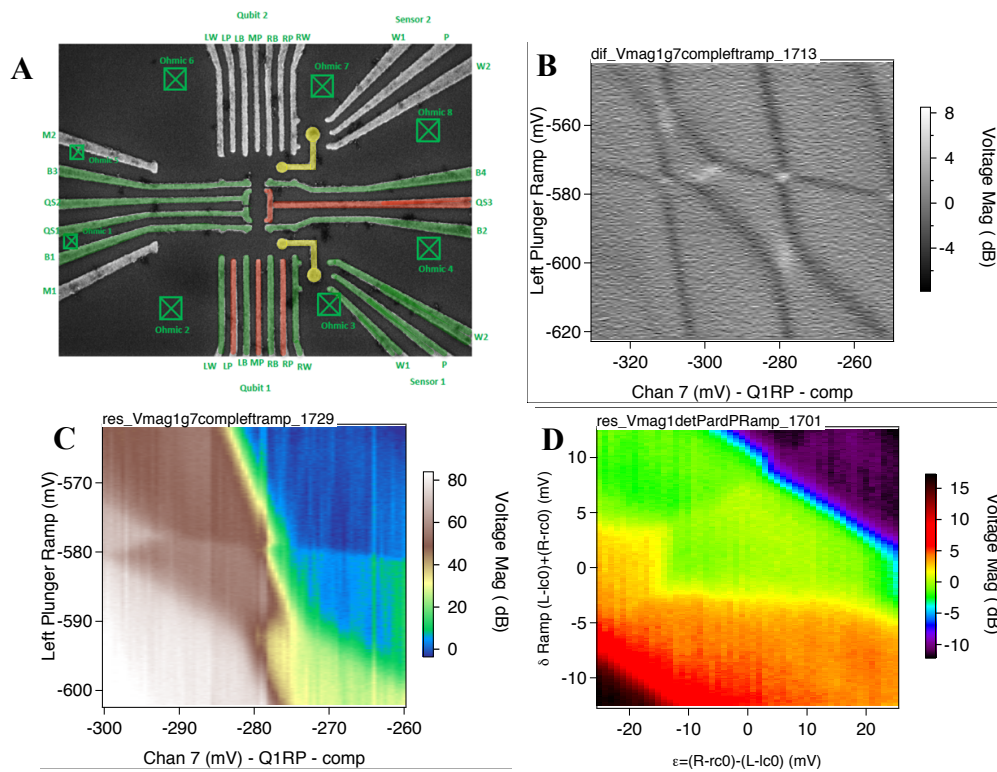


**Figure 31. Triple dot in Qubit 1 region.**

A. The SEM and schematics. B. The triple dot measured using the reflectometry, differentiated graph. 3 different slopes can be seen on the figure, which indicates that there are 3 quantum dots formed. C. “Nice house” region in reflectometry, not differentiated. D. The “house” region plotted in the detuning coordinate system (see Figure 6A).

#### 4.2.1 A triple dot

A triple dot was formed in Qubit 1 position (see Figure 31); the spacing between the Coulomb oscillations is different in all 3 dots, which indicates an asymmetrical system with different size of the dots (number of electrons in each dot). It was impossible to find spin blockade in any transition; the problem might have been high asymmetry in the system or the wrong value of tunnelling barriers. The dots were hard to tune and impossible to get down to one electron (due to latching and other unexpected phenomena).

#### 4.2.2 The multi-electron dot as a third dot

The large “sausage” dot in the middle was tuned up using transport from Ohmic 6 to Ohmic 4. The spacing between the found Coulomb oscillations indicates a large size of the dot. For a better visibility of the Coulomb oscillations at more depleted values, a charge sensor was needed. The oscillations in the dot were not detectable by the tuned up sensor in Sensor 1 position. For sensing of the transitions in the multi-electron dot, one of the dots in the Qubit 2 position was used as a charge sensor. The new sensor dot was closer to the “sausage” and Coulomb oscillations in the dot were detectable. The spacing between the Coulomb oscillations was too small to make sure that any position on the charge stability diagram would not drift into another state by small changes in the electrostatic surroundings of the dot (Figure 32). The dot was therefore brought into a

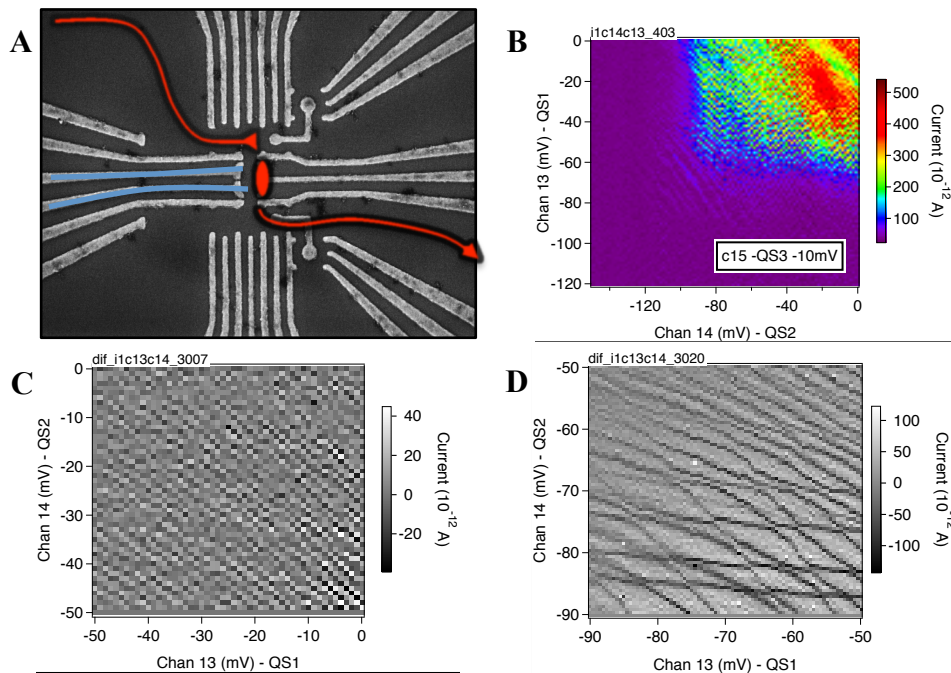


**Figure 32. The multi-electron dot.**

A. Micrograph of the device. B. Coulomb oscillations in the dot using the transport from ohmic 6 to ohmic 4. C. Charge sensing of the Coulomb oscillations using a dot in the Qubit 2 position. D. When applying larger voltage on the QS gates, the Coulomb oscillations in the dot show at least 3 different slopes, which indicates a splitting of the large dot into a number of smaller dots, caused by the depletion gates (probably the 2DEG was not even depleted underneath the QS gates, the value of the depletion underneath all other gates was around 100mV).

more depleted region in a search for more spaced Coulomb oscillations. Surprisingly, after changing the voltage of the depletion gates by no more than -50mV, the single dot in the sausage position had split into multiple dots, as seen in Figure 32.

The large multi-electron dot was intended for use as a third dot for the double dot shown in section 4.1. This “sausage” dot was present, while taking the double dot data, however, the multi-electron dot did not seem to be coupled to the double dot. First the large dot was tuned up and the tunnelling barrier left open towards the Qubit 1 region, then the double dot in the right and middle dots in Qubit 1 position (see the schematics in Figure 27) was tuned up. However, there was no coupling between the sausage dot and the double dot, both things were impossible to detect at the same time, which makes the experiment hard to proceed with. The coupling between the double dot and the sausage dot is quite hard to tune, since the tunnelling barrier for the multi-electron dot is at the same time the backbone for the double dot.

### **4.3 The coupler**

The metallic coupler gate did not seem to influence the dots formed in the Qubit 1 position. The occupancy of the dots was never brought down to zero electrons, however, there did not seem to be an evident difference between the left and the middle dots, where there was no metallic gate in the middle of the gate, and the right dot, where the metallic gate was placed directly on top of the quantum dot region. No unexpected phenomena were observed in the dots around the coupler gate.

The usual distance between the measured quantum dot and the sensor dot is approximately 500-600 nm. The distance from the sensor up to the farthest sensible dot in this design is around 700-800 nm. The metallic coupler might have improved the sensing, however, the distance is not significantly larger than usual, so no unambiguous conclusion can be drawn in this situation.

During the measurements, the sensor dot was strongly capacitively coupled to all three qubit dots. The right dot showed strongest coupling to the sensor, which added a strong background to the sensor measurements. The cross capacitance was compensated by stepping the plunger gate of the sensor by a percentage of the added voltage on the right plunger. The strong coupling between the sensor and the right dot gates can either be due to a very close distance between the right plunger and the sensor dot, or due to the coupler gate connecting the right dot with the sensor.

### **4.5 Summary of other experiences**

The primary goal for this study was performing the measurements described in the previous section. Aside from that, during the preparation and measurement phase, a

number of experiences were drawn, both with respect to the fabrication and operation of the devices. Those experiences are described in this section.

#### 4.4.1 Not working lines, the "sharp" pinch off

A number of samples were cooled down before a working device finally was found. Many devices failed because of the issue with bonding: bondwires kept being loose/broken, sometimes with no apparent reason (the bonds looked fine under the microscope). Since some of the devices were imaged on beforehand, there was a good certainty that the fine gates pattern definitely was all right. After taking the devices out of the fridge, the devices were imaged again, and still no gates seemed broken, neither under the optical microscope, nor under SEM. See Appendix B for a complete overview of the cooled down devices and failure modes.

Another problem associated with the performance of the depletion gates in the sharp pinch off, described in section 3.2 and shown in Figure 21B. Three of the cooled down devices showed similar behaviour (NO9d,e,g), no quantum dots could be formed in those devices. All 3 devices do have following things in common, that were changed for the next cooldowns:

- Micromagnets were fabricated on all 3 devices, and all of them were "melted".
- All these devices were imaged before the cooldown
- All these devices were cooled down on the newly received boards from Sydney and custom designed sample boards.
- The fact that those samples were taken from an edge of the wafer, where the doping might be different from the centre or uneven.

#### 4.4.2 Imaging

The imaging might have caused the sharp pinch off behaviour of the samples. In order to rule out this possibility, the same type of sample with magnets needs to be cooled down on Sydney board without imaging the device on beforehand. The results however might not be accurate if the actual cause of the sharp pinch off is due to uneven distribution of dopants on the piece of the wafer that the mentioned devices are cut out of.

An important note: while imaging the devices the surface of the wafer should be clean, with no resist residues. During the imaging process the devices are exposed to a large dose of e-beam. A normal dose for e-beam lithography is approximately  $2000 \mu\text{C}/\text{cm}^2$ , which breaks the polymer chains and allows them to be washed out during the development process. While exposure of and order of  $5000\text{-}7000 \mu\text{C}/\text{cm}^2$  can cause the cross-linking of the resist, which hardens the polymer chains and makes it the insoluble in the commonly used solvents. [44]. A hardened resist can actually be used for very fine lithography as a negative resist.

#### 4.4.3 Magnets

Unfortunately the original aim of this project could not be met due to the melted magnets. Those devices were measured anyway, but the depletion gates showed the sharp pinch-off behaviour. None of the non-magnetic samples were cooled down on the Sydney board, so the effect of the magnets cannot be ruled out completely. It is though unlikely that the magnets influenced the depletion behaviour of the devices. Additionally, all the previous studies that use micromagnets for spin qubits did show working quantum dots. For future devices the micromagnets must be fabricated as the last lithography step though.

#### 4.4.4 Boards

The new circuit boards from Sydney do have a big potential for future measurements. These boards were chosen for the first cooled down devices in order to characterise the boards and use all the new features that are implemented, including the smart disposable sample boards that can easily be interchanged without taking off the bonded devices. It is unfortunate that all the devices measured on the Sydney boards could not form quantum dots. The same type of boards are being used in Sydney for similar spin qubits experiments, which could lead to a conclusion that these boards most likely should work for the same types of wafers. The only unknown feature of these boards is the custom designed sample board; this factor could have influenced the measurements.

# Chapter 5. Summary and outlook

---

## 5.1 Summary of the results and experiences

A working fabrication recipe for the new Manfra materials was developed and proven reproducible. The fabricated devices did show promising results, though further study is needed to support the first results shown in this thesis. The floating metal gate connecting the sensor and the qubit quantum dots did not seem to disturb the quantum dot operations. Whether the gate improved the sensing can only be tested in the new devices either via designing the sensor farther away from the qubit, or by comparing sensors with and without a floating gate on the same chip. Given this technique works, it is a step towards individual sensing and readout of each qubit with big potential for scalability: the qubit operations can be sensed from a large distance, so the sensor does not have to be located near the qubit, which gives the space for more qubits. The technique can lead to fulfilment of a number of DiVincenzo criteria.

The large multi-electron quantum dot could be tuned up into a regime of dense Coulomb oscillations, which indicates the large size of the formed dot. When trying to find more spaced oscillations by shrinking the dot, the depletion gates broke the large dot into at least 3 separate dots by applying a relatively low voltage on the depletion gates around the dot. For more controlled manipulations of the large dot, the distance between the depletion gates needs to be increased. The multi-electron dot was impossible to sense with the intended sensors, the geometry needs to be changed in order to improve the sensing. The tunnelling barriers for the dot were at the same time backbone gates for the rest of the dots, which is not very practical either.

The magnetic field gradient looks like a promising tool for the spin qubit operations, however, none of the fabricated devices with magnets could be used because of the melted magnets. Improvement of the fabrication process by producing the magnets as the last step of fabrication would solve the problem. Covering of the magnets with a layer of gold could prevent the magnets from oxidising and might help with the melting problem as well.

The effect of SEM imaging is not yet understood: it is unknown, whether it actually damages the 2DEG material. The sharp pinch-off curves observed on multiple devices do suggest though that imaging might have an effect to the devices, though the results are not definitive. A more systematic study can reveal the effect of imaging; else the measured devices should remain “unimaged”.

Fabrication of fine gates can be done using single pixel lines, however, if the distance between the gates does not need to be less than 50nm, the single pixel line fabrication is not necessary. In any case, fabrication of the fine pattern should definitely be done on a more stable and reproducible system like Elionix. The Raith system can produce very fine features; the success rate is higher on Elionix though.

## 5.2 Suggestions for the improvements

Both the metallic coupler gate and the large “sausage dot” need improvements for further study. The placement of the sensor could be improved as well. A design suggestion of such a study is presented in Figure 33. There are 4 sensors. The left side should be sensed by either of the two left-side sensors. If the coupling gate functions as expected, both of the sensors should get the same signal from the left triple dot. If the coupler does not influence the sensing, the leftmost sensor should not be able to sense anything. The sensors to the right do not have a coupler, thus the signal from the right triple dot using the right sensors should be weaker than the signal from the left triple dot using the left sensors. If the signals are comparable, again, the coupler might not add much to the sensing.

One of the promising techniques for improving the device performance is applying a metallic gate on top of all the depletion gates (but not on top of the dots). The technique was suggested in Johannes Beil’s thesis [38] and did show promising results. A similar approach could be used for further devices for reducing the cross capacitance. Another interesting idea is placing an oxide layer underneath the depletion gates to get rid of all the possible leakage current. Placing an accumulation gate (opposite to depletion) right above the dot region is another interesting idea: by applying positive voltage above the dot region, a steeper potential for the dot can be achieved.

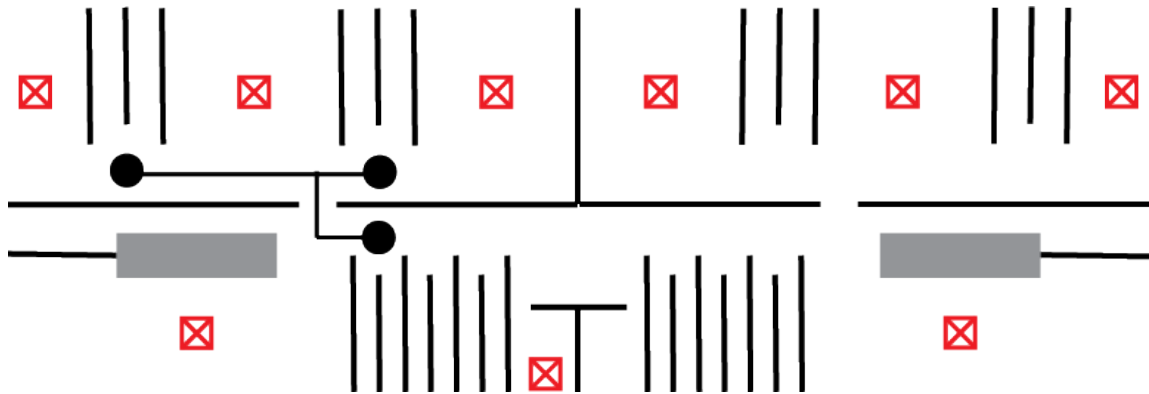


**Figure 33. Suggested geometry for further studies.**

In this geometry the effect of the metallic coupler can be tested. There is higher probability for sensing the “sausage” dot in this layout. This geometry is also more scalable, if the micro magnets can be placed directly on top of the depletion gates.

For better performance, a material with higher g-factor can be chosen for the spin qubit experiments. GaAs is widely used because of the well-established theoretical and reliable measurement data available. A different material might give even better results for future spin qubit devices.

For the scalability parameter in the DiVincenzo criteria: a new paradigm for forming and controlling the quantum dots is needed, top gating of GaAs is a good tool, however, if each dot needs at least 3 gates: two for the barriers in and out of the dot and one for the chemical potential, soon there would be not enough space for all the depletion gates, when scaling up to 5 and more qubits.

### **5.3 Conclusion**

A good design was developed for the experiments with two qubits that are driven using magnetic field gradient from a micromagnet. By adjusting the recipe for fabrication of the micromagnets, one can proceed with further experiments in this direction. Coupling of the two qubits with a multi-electron dot though might be a problem if using the designed gate layout: the control of the coupling between the multidot and the qubit can only be executed via the backbone gates for the qubit quantum dots. This is not practical and a linear design might be a better solution for this problem. The multi-electron quantum dot as a part of a qubit is still an open question, further measurements towards investigating this field are important for understanding the electron interactions in large quantum dots.

The results presented in this thesis did not fulfil the listed DiVincenzo criteria for the qubit suitable for quantum computations. However, this study brought us a little step closer towards building a quantum computer, as it also raised a number of questions that might serve a key to building a fault-tolerant quantum system and give a wider perspective on the spin physics of quantum dots.

## Appendix A. Fabrication Recipe

---

### Repeated actions

#### 3-solvent clean

- Ultrasonication in trichloroethylene (TCE) for 5 min
- Ultrasonication in Acetone for 5 min
- Ultrasonication in Isopropanol (IPA) for 5 min

#### Lift off

- Warm PG remover up to 85°C in the water bath or acetone up to 55°C
- Put the chip in, sonicate for 1 min
- Put the chip in fresh 85°C PG remover and leave on the water bath for 1 hour
- Ultrasonicate for 1 min
- Use a needle to spray the surface of the chip to remove last pieces of metal
- Rinse in IPA, N<sub>2</sub> dry

### Lithography steps developed for the E-line

---

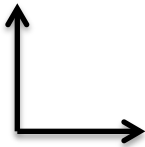
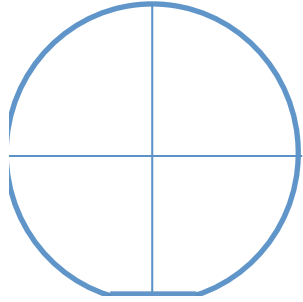
#### Exposing Ohmics or outer connection layer

- 3-solvent clean, N<sub>2</sub> blow dry
- Pre-bake on 185°C >2 min
- Rest on a glass slide for 15s to cool down
- Spin 9% Co-Polymer at 4000rpm, 4000rpm/s for 60s
- Bake on 185°C for minimum 3 min
- Rest on a glass slide for 60s to cool down
- Spin 4% PMMA (dissolved in anisole) at 4000rpm, 4000rpm/s for 60s
- Bake on 185°C for minimum 3 min
- Expose in the E-Line with 120µm aperture, 20kV
- Develop in MIBK:IPA 1:3 for 60s
- Rinse with oxygen plasma for 17s

#### Fine gates in the E-line

- 3-solvent clean, N<sub>2</sub> blow dry
- Pre-bake on 185°C >2 min
- Rest on a glass slide for 15s to cool down
- Spin 2% PMMA (dissolved in anisole) at 1500rpm, 4000rpm/s for 60s
- Bake on 185°C for minimum 5 min (to avoid collapse: bake for 1 hour)
- Expose in the E-line with 20µm aperture, 15kV, line dose 1000nA/cm, area dose 350
- Develop:
- Cool down pure IPA and IPA:H<sub>2</sub>O 7:3 solution on ice for 15 min. The temperature in both solutions should be approximately 2°C
- Develop 30s in cold IPA:H<sub>2</sub>O solution, 5s in cold IPA, both under strong sonication
- Blow dry with N<sub>2</sub>
- Rinse with oxygen plasma for 6s (the machine needs 3 s to create plasma, so the chip will get 3s)

Date: \_\_\_\_\_

<b>Sample name:</b>		<b>Wafer:</b>
<b>Sample orientation:</b>  	<b>Cleaved from:</b>  	
<b>Notes:</b>		

MESA PATTERNING						
	Junk chip			Real Chip		
	Name	Date	Comment	Name	Date	Comment
3 solvent clean, N <sub>2</sub> dry						
Pre-bake 5 min at 185°C						
Spin S1813 10s at 500rpm, 500rpm/s 60s at 4000rpm, 4000rpm/s						
Bake 2 min at 115°C						
Expose edges in mask aligner for 20s						
Develop: 60s in CD-26 20s in Mili-Q water						
Expose the mesa pattern in mask aligner for 16s						
Develop: 60s in CD-26 20s in Mili-Q water						
O <sub>2</sub> plasma ash for 10s						

MESA ETCH		
	Junk chip Name Date Comment	Real Chip Name Date Comment
Prepare H <sub>2</sub> SO <sub>4</sub> :H <sub>2</sub> O <sub>2</sub> :H <sub>2</sub> O 1:8:240		
Etch, wash in H <sub>2</sub> O	Time Bath H <sub>2</sub> O Temp	Time Bath H <sub>2</sub> O Temp
Sonicate in Acetone for 5 min and in IPA for 2 min, N <sub>2</sub> dry		
Determined Etch rate from the Junk Chip	Mesa Height on the real chip	
Warm the chip in PG remover/acetone and leave for 1-2 hours, O <sub>2</sub> plasma ash		
Take pictures of the mesa		

OHMICS PATTERNING			
	Name	Date	Comments
3 solvent clean, N <sub>2</sub> dry			
Bake 5 min 185°C Cool down 30s on glass slide			
Spin 9% Co-polymer 10s at 500rpm, 500rpm/s 60s at 4000rpm, 4000rpm/s			
Bake 3 min at 185°C, Cool down for 60s			
Spin 4% PMMA 10s at 500rpm, 500rpm/s 60s at 4000rpm, 4000rpm/s			
Bake 3 min at 185°C			
Expose in Elionix: <b>700 μC/cm<sup>2</sup></b>  Parameters: <i>100kV, 600μm writefield, 250 μm apt., 20.000 dots</i>			Current:  Dwell time:  Cont:  Brt:  Z:
Develop in MIBK:IPA 1:3 60s, rinse in IPA 5s, check in optical microscope			
O <sub>2</sub> plasma ash for 20s (23s)			

OHMICS DEPOSITION AND LIFT OFF																																																																			
	Name      Date      Comments																																																																		
Load the sample into AJA, let it stay in vacuum for 20min																																																																			
Ash with Ar plasma for 120s	<i>Note the Pressure</i>																																																																		
Deposit: (for approx. 50 nm depth) 43nm Ge 30nm Pt 87nm Au	<i>Note the rate. pressure</i>																																																																		
Lift Off in 55° Acetone for 2+ hours																																																																			
Anneal in RTA	<table border="1"> <thead> <tr> <th>Step</th> <th>Function</th> <th>Time (s)</th> <th>Temp degC</th> <th>N<sub>2</sub> (sccm)</th> <th>Forming gas (sccm)</th> </tr> </thead> <tbody> <tr><td>1</td><td>delay</td><td>20</td><td>0</td><td>5000</td><td>0</td></tr> <tr><td>2</td><td>delay</td><td>20</td><td>0</td><td>0</td><td>5000</td></tr> <tr><td>3</td><td>ramp</td><td>20</td><td>120</td><td>0</td><td>2000</td></tr> <tr><td>4</td><td>steady</td><td>60</td><td>120</td><td>0</td><td>2000</td></tr> <tr><td>5</td><td>ramp</td><td>20</td><td>250</td><td>0</td><td>2000</td></tr> <tr><td>6</td><td>steady</td><td>60</td><td>250</td><td>0</td><td>2000</td></tr> <tr><td>7</td><td>ramp</td><td>30</td><td>420</td><td>0</td><td>2000</td></tr> <tr><td>8</td><td>steady</td><td>120</td><td>420</td><td>0</td><td>2000</td></tr> <tr><td>9</td><td>delay</td><td>500</td><td>0</td><td>0</td><td>2000</td></tr> <tr><td>10</td><td>delay</td><td>30</td><td>0</td><td>5000</td><td>0</td></tr> </tbody> </table>	Step	Function	Time (s)	Temp degC	N <sub>2</sub> (sccm)	Forming gas (sccm)	1	delay	20	0	5000	0	2	delay	20	0	0	5000	3	ramp	20	120	0	2000	4	steady	60	120	0	2000	5	ramp	20	250	0	2000	6	steady	60	250	0	2000	7	ramp	30	420	0	2000	8	steady	120	420	0	2000	9	delay	500	0	0	2000	10	delay	30	0	5000	0
Step	Function	Time (s)	Temp degC	N <sub>2</sub> (sccm)	Forming gas (sccm)																																																														
1	delay	20	0	5000	0																																																														
2	delay	20	0	0	5000																																																														
3	ramp	20	120	0	2000																																																														
4	steady	60	120	0	2000																																																														
5	ramp	20	250	0	2000																																																														
6	steady	60	250	0	2000																																																														
7	ramp	30	420	0	2000																																																														
8	steady	120	420	0	2000																																																														
9	delay	500	0	0	2000																																																														
10	delay	30	0	5000	0																																																														
Take Pictures																																																																			
Test ohmics @ 4K																																																																			

FINE GATES PATTERNING	
3-solvent clean, N <sub>2</sub> dry	
O <sub>2</sub> plasma ash for 30s (33s)	
Pre-bake 4 min at 185°C, cool down 30s	
Spin 4% PMMA 10s at 500rpm, 500rpm/s 60s at 4000rpm, 4000rpm/s	
Bake 3 min at 185°C	
Expose in Elionix: <b>2400 <math>\mu\text{C}/\text{cm}^2</math></b>  Exposure parameters: <i>150<math>\mu\text{m}</math> writefield,</i> <i>60.000 dots, 500pA,</i> <i>40<math>\mu\text{m}</math> apert</i>	Current:  Dwell time:  Cont:  Brt:  Z:
Cool down MIBK:IPA 1:3 solution and separately IPA on ice for 15 min (temp approx. 2-3 deg C)	
Develop in MIBK:IPA for 90s w sonication (#1); rinse in cold IPA 10s and room temp. IPA for 20s, N <sub>2</sub> dry	
Check alignment, take pictures	

## FINE GATES DEPOSITION AND LIFT OFF

O2 plasma ash 6s (9s)	
Load the sample into AJA, leave it in vacuum for 20 min	
Deposit: 5nm Ti 15nm Au	<i>Note the rate, pressure</i>
Lift Off in hot Acetone/NMP for 2+ hours	
Take Pictures	
Notes:	

OUTER CONNECTION LAYER PATTERNING	
	Name      Date      Comments
3 solvent clean, N <sub>2</sub> dry	
Pre-bake 5 min at 185°C, cool down 30s	
Spin 9% Co+polymer 10s at 500rpm, 500rpm/s 60s at 4000rpm, 4000rpm/s	
Bake 3 min at 185°C, Cool down for 30s	
Spin 4% PMMA 10s at 500rpm, 500rpm/s 60s at 4000rpm, 4000rpm/s	
Bake 3 min at 185°C, observe under optical microscope	
Expose in Elionix: <b>770 <math>\mu\text{C}/\text{cm}^2</math></b> for innermost <b>700 <math>\mu\text{C}/\text{cm}^2</math></b> for outermost  Parameters: <i>100kV,</i> <i>600<math>\mu\text{m}</math> writefiel.,</i> <i>20.000 dots,</i> <i>250 <math>\mu\text{m}</math> apt., 40 nA</i> <i>for rough part</i> <i>120 <math>\mu\text{m}</math> apt., 5 nA</i> <i>for finer part</i>	Current:  Dwell time:  Cont:  Brt:  Z:
Develop in MIBK:IPA 1:3 for 60s, rinse in IPA for 5s	
Check the alignment, take pictures	
O <sub>2</sub> plasma ash for 17s (20s)	

**OUTER CONNECTION LAYER DEPOSITION AND LIFT OFF**

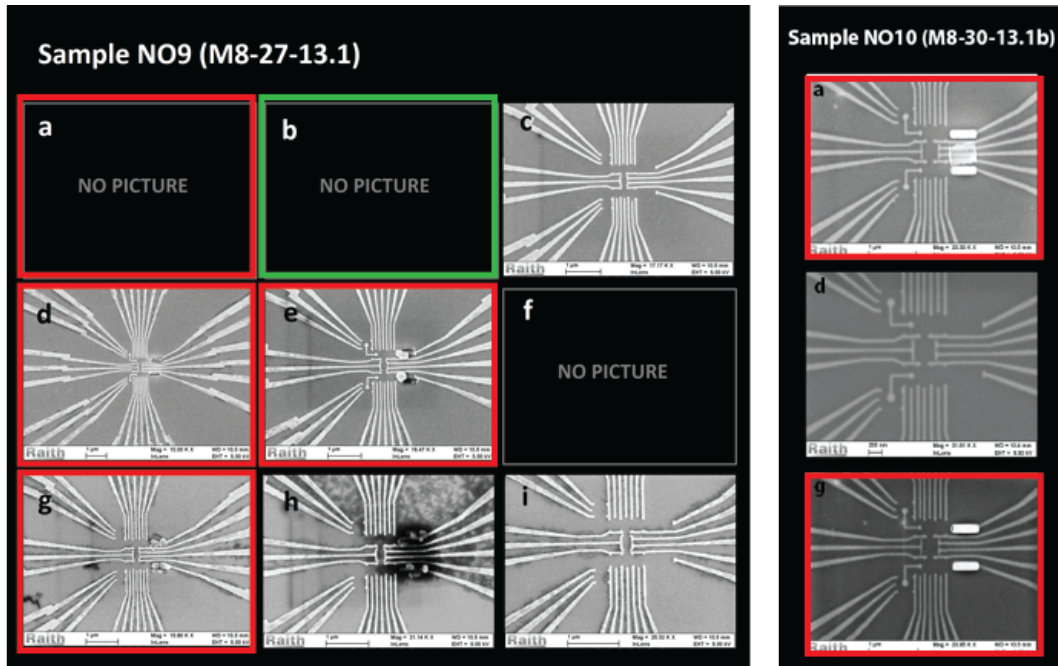
	Name	Date	Comments
Load the sample into AJA			
Deposit: (total of 1.2 x mesa height) 10nm Ti 110nm Au			<i>Note the rate, pressure</i>
Lift Off in 55° Acetone for 2+ hours			
Take Pictures			
Notes:			

MAGNETS PATERING	
3-solvent clean, N <sub>2</sub> dry	
O <sub>2</sub> plasma ash for 30s (33s)	
Pre-bake 4 min at 185°C, cool down 30s	
Spin 9% Co+polymer 10s at 500rpm, 500rpm/s 60s at 4000rpm, 4000rpm/s	
Bake 3 min at 185°C, Cool down for 30s	
Spin 4% PMMA 10s at 500rpm, 500rpm/s 60s at 4000rpm, 4000rpm/s	
Bake 3 min at 185°C	
Expose in Elionix: <b>2800 <math>\mu\text{C}/\text{cm}^2</math></b>  Exposure parameters: <i>150<math>\mu\text{m}</math> writefield,            60.000 dots, 100pA,            40<math>\mu\text{m}</math> apert</i>	. Current:  Dwell time:  Cont:  Brt:  Z:
Develop in MIBK:IPA 1:3 for 60s, rinse in IPA for 5s, N <sub>2</sub> blow dry	
Check alignment, take pictures	

## MAGNETS DEPOSITION AND LIFT OFF

O2 plasma ash 6s (9s)	
Load the sample into E-gun, leave it in vacuum for 20 min	
Deposit: 5nm Ti 100 nm Co 20 nm Au	<i>Note the rate, pressure</i>
Lift Off in hot Acetone/NMP for 2+ hours	
Take Pictures	
Status of finished device(s):	

## Appendix B. Cooled down devices, bonding schemes, boards



### Fabricated samples<sup>6</sup>

Table 3. Overview for the fabricated devices (not taken into account all the endless dosetestes):

Sample	Quantity	Wafer	Design	Faith
NO1	6 mesas	M6-9-12.1	15 in a row	Mesas were contaminated by the Ga from the backside of the wafer
NO2	6 mesas	M6-9-12.1	15 in a row	Ashed with Ar plasma
NO3	6 mesas	M6-6-12.1	15 in a row	Holes in mesa
NO4	6 mesas	M6-6-12.1	15 in a row	Ashed with Ar plasma
NO5	6 mesas	M8-27-13.1	15 in a row	Ashed with Ar plasma
NO6	6 mesas	M8-27-13.1	15 in a row	Broke into thousands of precious Manfra material pieces on the bottom of AJA1
NO7	6 mesas	M8-27-13.1	15 in a row	NO7a,b,f measured by Martin Kufahl and Peter Dahl Nissen, the rest is still unmeasured.
NO8	10 mesas	M8-27-13.1	Magnet	4 devices died due to lift-off, 6 others have some gates shorted due to the lift-off, but can still work.
NO9	9 mesas	M8-27-13.1	Magnet	All 9 ready, the measured ones are listed below
NO10	9mesas	M8-30-13.1b	Magnet	Only NO10a,d,g survived, NO10d broke over during cleaving, the other two were cooled down.

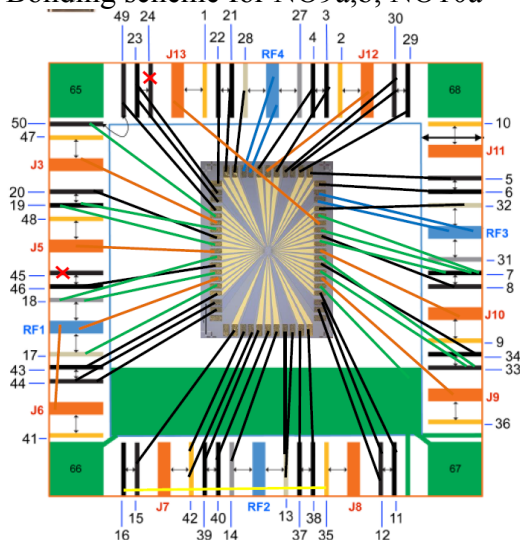
<sup>6</sup> NO1-NO7 made in collaboration with Peter Dahl Nissen

## The cooled down devices<sup>7</sup>

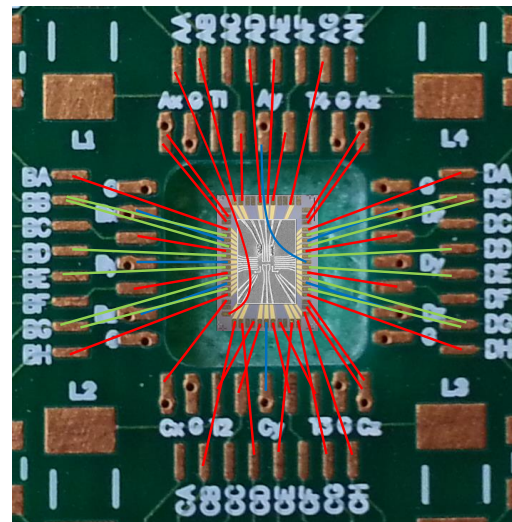
Table 4. Overview for the cooled down devices, data presented in this thesis is mostly taken on NO9b.

Device	Board	Imaged	Magnets	Comments
NO7a	Mayo	no	no	Could form dots, geometry was not optimal though
NO7b	Mayo	no	no	Gates blown up
NO7f	Mayo	no	no	Gates blown up
NO9a	Mayo	no	no	Could form dots, some of the bonds or gates broken
NO9b	Mayo	no	no	Could form dots, data presented in this thesis
NO9d	Sydney	yes	yes	Some of the gates showed sharp pinch off, some of the gates/bonds were broken, magnets melted
NO9e	Sydney	yes	yes	Some of the gates showed sharp pinch off, some of the gates/bonds were broken, magnets melted
NO9g	Sydney	yes	yes	Some of the gates showed sharp pinch off, some of the gates/bonds were broken, magnets melted
NO10a	Mayo	yes	no	Cross-linked resist. Was bonded to a Mayo board with contaminated pads, there was no contact to the most of the gates.
NO10g	Sydney	yes	no	Cross-linked resist. Single gates could pinch off the transport through the device, which should not happen!

Bonding scheme for NO9a,b, NO10a



Bonding scheme for NO9d, e, g, NO10g

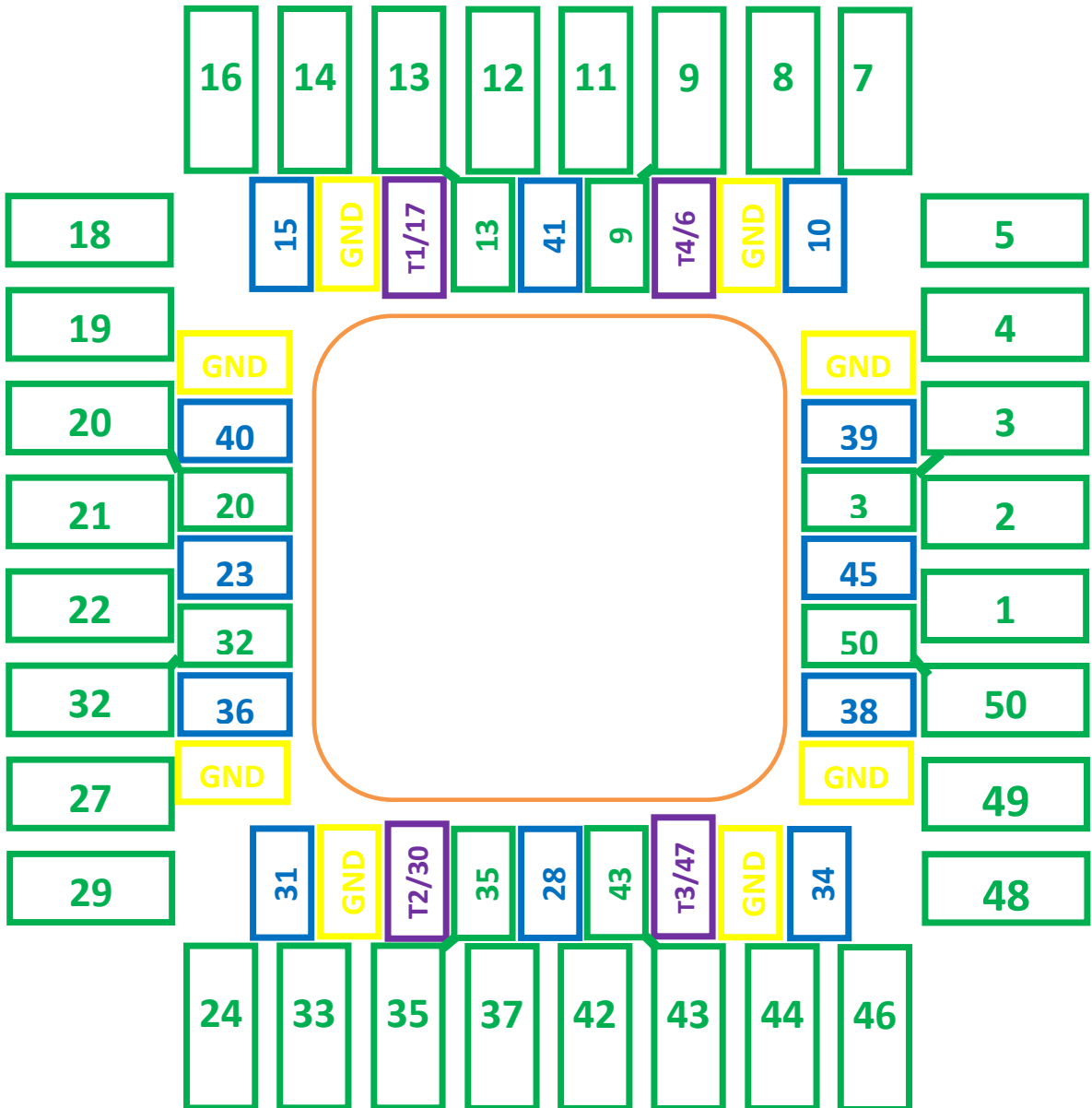


<sup>7</sup> NO7 devices are measured by Martin Kufahl and Peter Dahl Nissen, data from the measurements presented in Martin Kufahl's master thesis.

## Appendix C. Pin-out for the Sydney board

**Green** – DC lines  
**Blue** – DC lines connected to a coax line via a bias tee  
**Yellow** – ground  
**Purple** – tank circuits  
**NC** – not connected

view onto male 51 nano-D connector (J1 / J2):



## Bibliography

1. Ladd, T.D., *Quantum Computing*. Nature, 2010. **464**: p. 45-53.
2. D.P.DiVincenzo, *The Physical Implementation of Quantum Computation*. 2000.
3. Wiesner, S., *Conjugate coding*. SIGACT News, 1983. **15**(1): p. 78-88.
4. Shor, P., *Scheme for reducing decoherence in quantum computer memory*. Physical Review A, 1995. **52**(4): p. R2493-R2496.
5. Loss, D. and D. DiVincenzo, *Quantum computation with quantum dots*. Physical Review A, 1998. **57**(1): p. 120-126.
6. Hanson, R., et al., *Spins in few-electron quantum dots*. Reviews of Modern Physics, 2007. **79**(4): p. 1217-1265.
7. Press, D., et al., *Complete quantum control of a single quantum dot spin using ultrafast optical pulses*. Nature, 2008. **456**(7219): p. 218-221.
8. Petta, J.R., et al., *Coherent Manipulation of Coupled Electron Spins in Semiconductor Quantum Dots*. Science, 2005. **309**(5744): p. 2180-2184.
9. Medford, J., et al., *Quantum-Dot-Based Resonant Exchange Qubit*. Physical Review Letters, 2013. **111**(5): p. 050501.
10. Medford, J., et al., *Self-consistent measurement and state tomography of an exchange-only spin qubit*. Nat Nano, 2013. **8**(9): p. 654-659.
11. M.A. Nielsen, I.L.C., *Quantum Computation and Quantum Information*. 2000: Cambridge University Press.
12. Medford, J.R., *Spin Qubits in Double and Triple Quantum Dots*, in *The Department of Physics*. 2013, Harvard University.
13. Barthel, C., *Control and fast Measurement of Spin Qubits*, in *The Department of Physics*. 2010, Harvard University.
14. von Delft, J. and D.C. Ralph, *Spectroscopy of discrete energy levels in ultrasmall metallic grains*. Physics Reports, 2001. **345**(2-3): p. 61-173.
15. Petta, J.R. and D.C. Ralph, *Studies of Spin-Orbit Scattering in Noble-Metal Nanoparticles Using Energy-Level Tunneling Spectroscopy*. Physical Review Letters, 2001. **87**(26): p. 266801.
16. Park, J., et al., *Coulomb blockade and the Kondo effect in single-atom transistors*. Nature, 2002. **417**(6890): p. 722-725.
17. Guéron, S., et al., *Tunneling via Individual Electronic States in Ferromagnetic Nanoparticles*. Physical Review Letters, 1999. **83**(20): p. 4148-4151.
18. Scholze, A., A. Schenk, and W. Fichtner, *Single-Electron Device Simulation*. IEEE, 2000. **47**(10): p. 1811-1818.
19. Barthel, C., et al., *Fast sensing of double-dot charge arrangement and spin state with a radio-frequency sensor quantum dot*. Physical Review B, 2010. **81**(16): p. 161308.
20. Takakura, T., et al., *Single to quadruple quantum dots with tunable tunnel couplings*. Applied Physics Letters, 2014. **104**(11): p. -.
21. Hanson, R. and D.D. Awschalom, *Coherent manipulation of single spins in semiconductors*. Nature, 2008. **453**(7198): p. 1043-1049.
22. Trifunovic, L., et al., *Long-Distance Spin-Spin Coupling via Floating Gates*. Physical Review X, 2012. **2**(1): p. 011006.
23. Ritz, T., et al., *Resonance effects indicate a radical-pair mechanism for avian magnetic compass*. Nature, 2004. **429**(6988): p. 177-180.
24. Foletti, S., et al., *Universal quantum control of two-electron spin quantum bits using dynamic nuclear polarization*. Nat Phys, 2009. **5**(12): p. 903-908.

25. Koppens, F.H.L., et al., *Driven coherent oscillations of a single electron spin in a quantum dot*. Nature, 2006. **442**(7104): p. 766-771.
26. Pioro-Ladriere, M., et al., *Electrically driven single-electron spin resonance in a slanting Zeeman field*. Nat Phys, 2008. **4**(10): p. 776-779.
27. Tokura, Y., et al., *Coherent Single Electron Spin Control in a Slanting Zeeman Field*. Physical Review Letters, 2006. **96**(4): p. 047202.
28. Pioro-Ladrière, M., et al., *Micromagnets for coherent control of spin-charge qubit in lateral quantum dots*. Applied Physics Letters, 2007. **90**(2): p. -.
29. Shin, Y.-S., et al., *Single-Spin Readout in a Double Quantum Dot Including a Micromagnet*. Physical Review Letters, 2010. **104**(4): p. 046802.
30. Obata, T., et al., *Coherent manipulation of individual electron spin in a double quantum dot integrated with a micromagnet*. Physical Review B, 2010. **81**(8): p. 085317.
31. Wu, X., et al., *Two-axis control of a singlet–triplet qubit with an integrated micromagnet*. Proceedings of the National Academy of Sciences, 2014. **111**(33): p. 11938-11942.
32. Laird, E.A., et al., *Coherent spin manipulation in an exchange-only qubit*. Physical Review B, 2010. **82**(7): p. 075403.
33. Brouwer, P.W., Y. Oreg, and B.I. Halperin, *Mesoscopic fluctuations of the ground-state spin of a small metal particle*. Physical Review B, 1999. **60**(20): p. R13977-R13980.
34. Srinivasa, V., H. Xu, and J.M. Taylor, *Tunable Spin Qubit Coupling Mediated by a Multi-Electron Quantum Dot*. arXiv.org, 2013. **cond-mat.mes-hall**.
35. Ihn, T., *Semiconductor nanostructures: Quantum states and electronic transport*. 2010.
36. Nowack, K.C., et al., *Coherent Control of a Single Electron Spin with Electric Fields*. Science, 2007. **318**(5855): p. 1430-1433.
37. Kufahl, M., *Experimental Methods for Implementing Electron Spin Qubits in Double Quantum Dots*, in *Center for Quantum Devices*. 2014, University of Copenhagen.
38. Beil, J., *Towards the coherent coupling of multiple three-electron spin-qubits*, in *Center for Quantum Devices*. 2014, University of Copenhagen.
39. MicroChem, *NANO™ PMMA and Copolymer*, in *PMMA Data Sheet*. 2001.
40. Tanaka, N. and T. Ishikawa, *Energy dependence and depth distribution of electron beam-induced damage in GaAs/AlGaAs heterostructures*. Journal of Electronic Materials, 1994. **23**(3): p. 341-346.
41. Fink, T., D.D. Smith, and W.D. Braddock, *Electron-beam-induced damage study in GaAs-AlGaAs heterostructures as determined by magnetotransport characterization*. Electron Devices, IEEE Transactions on, 1990. **37**(6): p. 1422-1425.
42. Kleiber, M., et al., *Magnetization switching of submicrometer Co dots induced by a magnetic force microscope tip*. Physical Review B, 1998. **58**(9): p. 5563-5567.
43. Reilly, D.J., et al., *Fast single-charge sensing with a rf quantum point contact*. Applied Physics Letters, 2007. **91**(16): p. -.
44. Zailer, I., et al., *Crosslinked PMMA as a high-resolution negative resist for electron beam lithography and applications for physics of low-dimensional structures*. Semiconductor Science and Technology, 1996. **11**(8): p. 1235.